geosciences

MDPI

Article

Cenozoic Carbon Dioxide: The 66 Ma Solution

Patrick Frank

SLAC National Accelerator Laboratory, Stanford University, Menlo Park, CA 94025, USA; pfrank@slac.stanford.edu

Abstract: The trend in partial pressure of atmospheric CO_2, $P(CO_2)$, across the 66 MYr of the Cenozoic requires elucidation and explanation. The Null Hypothesis sets sea surface temperature (SST) as the baseline driver for Cenozoic $P(CO_2)$. The crystallization and cooling of flood basalt magmas is proposed to have heated the ocean, producing the Paleocene–Eocene Thermal Maximum (PETM). Heat of fusion and heat capacity were used to calculate flood basalt magmatic Joule heating of the ocean. Each 1 million km^3 of oceanic flood basaltic magma liberates ~5.4×10^{24} J, able to heat the global ocean by ~0.97 °C. Henry's Law for CO_2 plus seawater (H_S) was calculated using $\delta^{18}O$ proxy-estimated Cenozoic SSTs. H_S closely parallels Cenozoic SST and predicts the gas solute partition across the sea surface. The fractional change of Henry's Law constants, $\frac{H_n - H_i}{H_n - H_0}$ is proportional to $\Delta P(CO_2)_i$, and $\frac{H_n - H_i}{H_n - H_0} \times \Delta P(CO_2) + P(CO_2)_{min}$, where $\Delta P(CO_2) = P(CO_2)_{max} - P(CO_2)_{min}$, closely reconstructs the proxy estimate of Cenozoic $P(CO_2)$ and is most consistent with a 35 °C PETM ocean. Disparities are assigned to carbonate drawdown and organic carbon sedimentation. The Null Hypothesis recovers the glacial/interglacial $P(CO_2)$ over the VOSTOK 420 ka ice core record, including the rise to the Holocene. The success of the Null Hypothesis implies that $P(CO_2)$ has been a molecular spectator of the Cenozoic climate. A generalizing conclusion is that the notion of atmospheric CO_2 as the predominant driver of Cenozoic global surface temperature should be set aside.

Keywords: null hypothesis; Henry's law; Cenozoic CO_2; Paleocene–Eocene Thermal Maximum; Miocene thermal optimum

check for updates

Citation: Frank, P. Cenozoic Carbon Dioxide: The 66 Ma Solution. *Geosciences* **2024**, *14*, 238. https://doi.org/10.3390/geosciences14090238

Academic Editors: Deodato Tapete and Ronald W. Klusman

Received: 23 July 2024
Revised: 26 August 2024
Accepted: 29 August 2024
Published: 3 September 2024

Copyright: © 2024 by the author. Licensee MDPI, Basel, Switzerland. This article is an open access article distributed under the terms and conditions of the Creative Commons Attribution (CC BY) license (https://creativecommons.org/licenses/by/4.0/).

1. Introduction

The sources, sinks, levels, and climatological consequences of atmospheric carbon dioxide over the Cenozoic remain a matter of considerable discussion [1–9]. The Paleocene–Eocene Thermal Maximum, 56 to 52 million years before the present (PETM, 56 to 52 MYr BP), and the Miocene Climate Optimum (MCO, 17 to 13 MYr BP) saw elevated sea surface temperatures (SSTs) and high levels of atmospheric CO_2. Sources of increased Cenozoic CO_2 have been ascribed to tectonic outgassing, to volcanic flood basaltic eruptions, and to a bolide impact [10–12]. Sinks have primarily been found in increased mineral weathering, especially of tectonically emergent surfaces, as well as extensive blooms of coccolithophores, increased photosynthetic fixation, and sedimentation of organic carbon [3,13–31]. For comprehensive reviews, see Wallmann, and Li et al. [31,32].

The inferred history of the Cenozoic climate has generally been interpreted in terms of the greenhouse impacts of greater or lesser partial pressures of atmospheric CO_2, $P(CO_2)$ [10,33–37]. However, efforts to model the Cenozoic climate have had difficulty reconciling the forcing of elevated Cenozoic CO_2 with the climate sensitivity of the models [7,33,38,39].

Seawater itself has not been evaluated as the source or sink of the changes in $P(CO_2)$ over the Cenozoic. The solubility of CO_2 in the world ocean varies inversely with sea surface temperature (SST). Therefore, $P(CO_2)$ should vary likewise, because the gas solute partition of CO_2 re-equilibrates across the sea surface as SST varies over geological time.

Henry's Law has long been used to find the partial pressure of a soluble gas in equilibrium with its dissolved congener [40,41]. Henry's Law constants are temperature dependent, and those for aqueous solutions are affected by electrolyte solutes [42–44]. Salinity modifies the specific solubility of CO_2 in seawater at a given $P(CO_2)$ and temperature. Henry's Law constants for seawater, along with their temperature dependence, have been determined [45–47].

This work derives a Null Hypothesis to explicate the variations in partial pressure of Cenozoic carbon dioxide. The Null Hypothesis proposes that precursory changes in SST governed the baseline level of $P(CO_2)$. A mechanism for the heating of the world ocean prior to $P(CO_2)$ elevation is described. The Null Hypothesis is based on Henry's Law, and is used herein to estimate the level of and variation in atmospheric $P(CO_2)$ over the 66 million years (Ma) of the Cenozoic.

2. Sources and Methods

2.1. Data Sources

The estimates of Cenozoic surface temperature and of atmospheric carbon dioxide were obtained from published sources [2,33]. The $\delta^{18}O$ proxy surface temperatures are accepted as representative of the sea surface within the limits of the method [48–50]. The $P(CO_2)$ of the Pleistocene was taken as the mean of the 800 ka EPICA Dome C record [51,52]. Historical (1750–2017) levels of atmospheric CO_2 were obtained from the Data Visualization site of the European Environmental Agency [53]. Temperature-dependent properties of seawater, including vapor pressure, were obtained from the "Standard seawater properties at 1 °C increment" published by the ITTC Corporation, Zurich, Switzerland [54].

2.2. Henry's Law Constants for 35.1‰ Salinity Sea Water

Temperature-varying Henry's Law constants for CO_2 gas over pure water were calculated using polynomial Equation (1), of Carroll, Slupsky, and Mather [55],

$$\ln(H_0) = -6.8346 + 1.2817 \times 10^4/T - 3.7668 \times 10^6/T^2 + 2.997 \times 10^8/T^3, \quad (1)$$

where H_0 is Henry's Law constant for CO_2 gas equilibrating across a surface of pure water and T is temperature in Kelvin.

2.3. Seawater Ions for 35.1‰ Salinity

The published ionic composition of mean seawater was approximated as Na^+, K^+, Mg^{2+}, and Ca^{2+} cations and Cl^- and $(SO_4)^{2-}$ anions [56]. All salts were assumed fully dissociated. The ionic concentrations were combined to achieve electroneutrality. The overall concentrations were then re-scaled to produce 35.1‰ salinity (35.1 g/kg). Other seawater ions make relatively minor contributions to salinity.

Molalities were calculated using the partial molal volumes of ions in seawater [57]. The total volume change on dissolution of the salts listed in Table 1 is 9.773 mL. Of this solution, 1 kg will contain 35.1 g of dissolved salts and 964.9 mL (53.606 moles) of water. The total volume of 1 kg of this solution is 964.9 mL + 9.773 mL = 974.673 mL. The density of this solution would be 1.026 g/mL. In comparison, the density of surface seawater varies globally with temperature, increasing from about 1.020 g/mL at the equator to 1.029 g/mL at the poles [58].

Table 1. Salts used to approximate seawater of 35.1‰ salinity [56].

Salt	NaCl	KCl	$MgCl_2$	$MgSO_4$	$CaSO_4$
Molality	0.472	0.0103	0.0336	0.0196	8.82×10^{-3}
g/kg	27.58	0.766	3.19	2.36	1.20
Molarity	0.456	0.0100	0.0324	0.0190	8.85×10^{-3}
Total mole fraction	8.716×10^{-3}	1.902×10^{-4}	6.205×10^{-4}	3.620×10^{-4}	1.629×10^{-5}
Mole fraction of salts	0.867	0.0189	0.0617	0.0360	0.0162

Total salinity: 35.1 g/kg = 35.1‰; total salt moles/kg = 0.544. Total mole fraction = (moles of salt)/(total moles) where total moles = (salts + water) = 54.150 moles/kg.

2.4. Weighting for the Least Squares Fit, $\Delta H_i/\Delta H_n$ vs. $\Delta P(CO_2)_i/\Delta P(CO_2)_n$

The greater density of points in the lower interval data overweighted the fit. Therefore, the linear least squares fit was weighted to normalize the varying number of points in each 0.1 interval of $\Delta P(CO_2)_i/\Delta P(CO_2)_n$. The applied weights (1/normalization factor)^2 are provided in Table S1 of the Supporting Information.

2.5. Data Analysis

Data were analyzed using the Kaleidagraph v. 5.0.4 analytics package (Synergy Software, Reading, PA, USA). Carbonate speciation was carried out using Medusa v. 1 software [59]. Data were digitized from published graphics using the program DigitizeIt v. 2.5.9 (I. Bormann, Braunschweig, Germany).

3. Results

3.1. Schumpe Parameters, the Sechenov Equation, and Henry's Law for CO_2 in Seawater

The Henry's Law constants for pure water were modified for seawater using the Sechenov equation and the Schumpe parameters (Table 2), using the associated equations for the major seawater ions (see Table 1 in Section 2) [44]. The Henry's Law analysis proceeded assuming the accuracy of estimated Cenozoic sea surface temperatures [33,60].

Table 2. Schumpe parameters for major seawater ions.

Anion	Schumpe h_i	Cation	Schumpe h_i
Cl^-	0.0318	Na^+	0.1143
SO_4^{2-}	0.1117	K^+	0.0922
		Mg^{2+}	0.1694
		Ca^{2+}	0.1762

Ion-specific Schumpe parameters are available in Table 5.5 of Abbatt (2019) [44].

The Sechenov equation modifies Henry's Law constants to account for dissolved salts in seawater [44]:

$$\log(H_0/H_S) = K_S \times c_S, \quad (2)$$

where H_0 is the Henry's Law constant for pure water and H_S is that for seawater, K_S is the Sechenov proportionality constant for seawater, and c_S is the ion concentration in M (M is molarity). The Sechenov proportionality constant is calculated as follows:

$$K_S = \Sigma(h_i + h_G) \times n_i, \quad (3)$$

where h_i is the Schumpe ion-specific constant, h_G is the gas-specific constant (CO_2), and n_i is the ion index defined as M_{ion}/M_{salt}. For the ions of Table 2, n_i(Cl) = 1.065, while the remainder are unity.

The h_G parameter is modified by h_T to include the temperature dependence of the Henry's Law constant:

$$h_G = h_{G,0} + h_T \times (T - 298.15\ \text{K}), \quad (4)$$

where T is in Kelvin. For carbon dioxide, H_0 (298 K) = 3.38 × 10^{-2} M/atm, $h_{G,0}$ = −1.72 × 10^{-2} M^{-1}, and h_T = −0.336 × 10^{-3} $M^{-1}K^{-1}$ [44]. Equation (4) was then used with the estimated Cenozoic surface temperature to calculate h_G for the entire Cenozoic time series [33].

Finally, the individual $K_{S(\text{ion})} \times c_{(\text{ion})}$ parameter (Equation (3)) was calculated for each ion at each temperature. These were summed to yield the sequential values of $K_{seawater} \times c$ across the Cenozoic temperature series. Then, from Equation (2):

$$\log(H_0/H_S) = K_{seawater} \times c. \text{ and } H_S = H_0/10^{Kseawater \times c}. \quad (5)$$

The Henry's Law constants for the estimated Cenozoic sea surface temperatures (SSTs) were thereby in hand. Figure 1 plots the calculated Henry's Law constant for seawater, H_S, and the $\delta^{18}O$ proxy estimate of Cenozoic sea surface temperature [33].

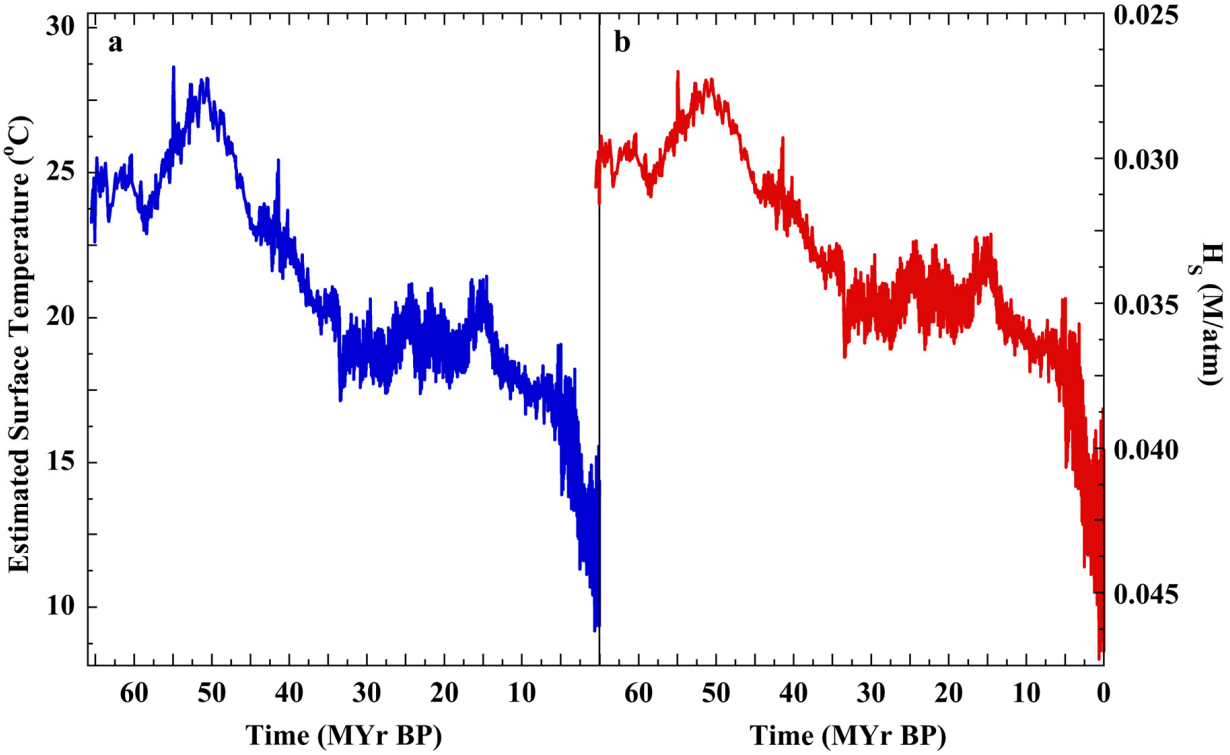


Figure 1. Cenozoic times series plot of (**a**) (blue line), the $\delta^{18}O$ proxy estimate of Cenozoic sea surface temperature, T_S [33]; (**b**) (red line), calculated Henry's Law constant for seawater, H_S, plotted with the ordinate decreasing upward. H_S varies with Cenozoic T_S.

The Henry's Law constant for seawater, H_S, closely varies with T_S over the entire 66 Ma Cenozoic time series.

The next section discusses the application of this result to reconstruct the ppm of atmospheric CO_2 over the Cenozoic, under the Null Hypothesis that Cenozoic SST was the driver of P(CO_2).

3.2. Henry's Law Estimation of Cenozoic CO_2

Here, CO_2 is appraised at the gas–seawater interface. Total CO_2 = $(CO_2)_{gas}$ + $(CO_2)_{ocean}$ is assumed to apply across the entire Cenozoic, where $(CO_2)_{ocean}$ is the neutral molecular form of dissolved CO_2 within the oceanic reservoir that is in equilibrium with the atmospheric gas phase. The approach begins with the relation between the Henry's Law

constant and the partition of a soluble molecule between gas and solute across the surface of a solvent, which is aqueous in this case [55].

$$x_i H = y_i \oint P \tag{6}$$

where x_i is the mole fraction of gas dissolved in solution, y_i is the mole fraction in the gas phase, $\oint$ is the fugacity coefficient, H is Henry's Law constant, and P is total pressure. Moles of CO_2 in the gas phase m_g, or as a solute m_s, enter the mole fraction as $m_g/(m_g + m_s)$ and $m_s/(m_g + m_s)$, respectively.

At low concentration,

$$\oint = 1, x_i H = y_i P and y_i/x_i = H/P. \tag{7}$$

Mole fractions sum to unity. From Equation (7):

$$P \times (y_i/x_i) = H \tag{8}$$

When P is total pressure, $P \times y_i = \mathrm{P(CO_2)}_i$, Equation (8) becomes $\mathrm{P(CO_2)}_i/x_i = H_i$, where $\mathrm{P(CO_2)}_i$is the partial pressure of solution-phase CO_2 at the ith point in a series, and $\mathrm{H_i}$ is the Henry's Law constant for the ith point [42].

Cenozoic $\mathrm{P(CO_2)}_i/x_i$ is unknown. However, it is known that $\mathrm{P(CO_2)}/x$ determines $\mathrm{P(CO_2)_{atm}}$. That is, given the sea surface temperature series $T_0, \ldots, T_i, \ldots, T_n$, over the Cenozoic, for each time instance t_i with temperature T_i, $\mathrm{P(CO_2}/x)_i = H_i$. Further, the Null Hypothesis assumes SST determines $\mathrm{P(CO_2)}$, such that at each instance of $t_i \rightarrow t_{i+1} = \Delta t_i$, the relation $\Delta \mathrm{P(CO_2}/x)_i = \Delta H_i \propto \Delta \mathrm{P(CO_2)}_i$ follows.

The fractional change ratios among $\mathrm{P(CO_2}/y)$, H_S, and $\mathrm{P(CO_2)}$ are therefore equatable. That is,

$$\frac{(\mathrm{P(CO_2)/x})_0 - (\mathrm{P(CO_2)/x})_\mathrm{i}}{(\mathrm{P(CO_2)/x})_0 - (\mathrm{P(CO_2)/x})_\mathrm{n}} = \frac{\mathrm{H_0 - H_i}}{\mathrm{H_0 - H_n}} = \frac{\mathrm{P(CO_2)_0 - P(CO_2)_i}}{\mathrm{P(CO_2)_0 - P(CO_2)_n}}, \tag{9}$$

where subscript '0' indicates the initial value, subscript 'i' references the ith value, and subscript 'n' indicates the final value. Each term in Equation (9) represents a fractional change attending an SST, $\mathrm{P(CO_2)}$ series traversing time points $\mathrm{t_o}, \ldots, \mathrm{t_i}, \ldots, \mathrm{t_n}$. Equation (9) operates under the assumption that SST governs $\mathrm{P(CO_2)}$.

3.3. Empirical Test of Henry's Law Ratios

The relationships of Equation (9) were empirically tested using the historical CO_2 and SST records. The modern record departs from constant $[\mathrm{CO_2}]_\mathrm{total}$ and thus constitutes a strong challenge, where the brackets ([]) indicate concentration.

For the test of Equation (9), the historical SST (1850–2017) was reconstructed by adding the ERSST v5 1961–1990 global mean sea surface temperature (18.9 °C) to the HadSST v.4.0.1.0_annual_GLOBE anomalies [61–63]. The appropriate Henry's Law constants for seawater were derived by interpolation of the Cenozoic SST $\mathrm{H_S}$ series (*cf.* Figure 1) onto the historical SSTs. The fractional ratios of Equation (9) were then calculated and are displayed in Figure 2.

Figure 2a shows the coherence of the three ratios over the historical period, as predicted by Equation (9). In Figure 2b, H/P is linearly correlated with the historical atmospheric $\mathrm{P(CO_2)}$ record, indicating that the gas/solute mole fraction varies directly with $\mathrm{P(CO_2)}$. Finally, Figure 2c shows slopes of 1.00 for the Equation (9) correlation plots with $\frac{\mathrm{H_0 - H_i}}{\mathrm{H_0 - H_n}}$. Specifically, the complete linearity of $\Delta \mathrm{H_{0,i}}/\Delta \mathrm{H_{0,n}}$ vs. $\Delta \mathrm{P(CO_2)_{0,i}}/\Delta \mathrm{P(CO_2)_{0,n}}$ empirically establishes the validity of employing the fractional change of Henry's Law constant with SST, to discover the fractional change in $\mathrm{P(CO_2)}$ as driven by SST.

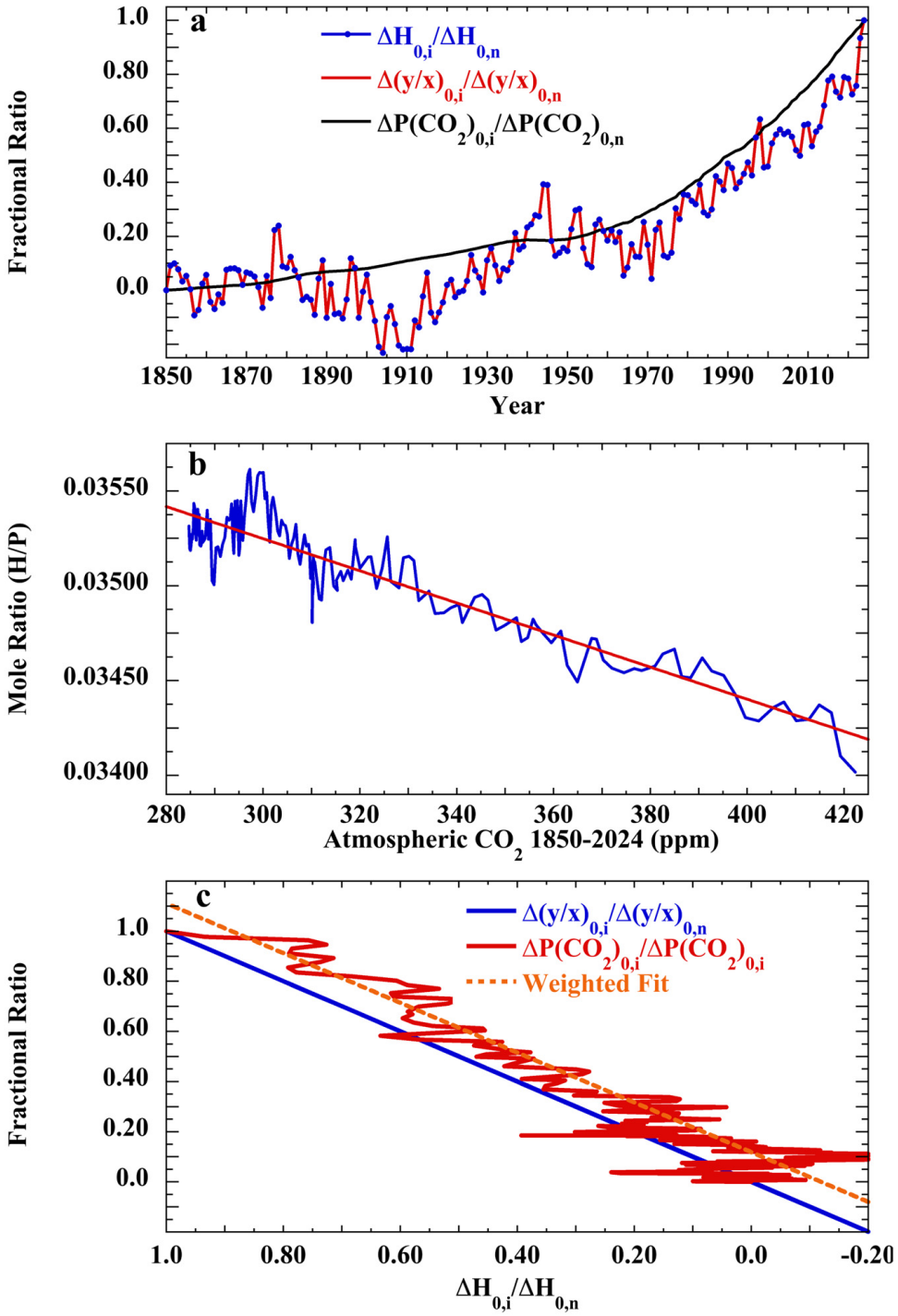


Figure 2. (**a**) $\frac{H_0-H_i}{H_0-H_n}$, (blue points); $\frac{(P(CO_2)/x)_0-(P(CO_2)/x)_i}{(P(CO_2)/x)_0-(P(CO_2)/x)_n}$, (red line); $\frac{P(CO_2)_0-P(CO_2)_i}{P(CO_2)_0-P(CO_2)_n}$, (black line); where $P(CO_2)$ is the historical atmospheric time series (ppm) since 1850. (**b**) (Blue line), Henry's Law constant divided by the historical atmospheric CO_2 time series plotted against CO_2 (ppm). The structure reflects the impact of the natural variation of SST on the Henry's Law constants (cf. h_G in Equation (4)); (red line), linear least squares fit: $H/P = 0.03779 - 8.466 \times 10^{-6} \times CO_2$ (ppm); $r^2 = 0.84$. (**c**) $\frac{P(CO_2)_n-P(CO_2)_i}{P(CO_2)_n-P(CO_2)_0}$, (red line), where $P(CO_2)$ is the historical record in ppm; (dashed red line), weighted fit through the data (see Sources and Methods Section); $\frac{(H/P)_n-(H/P)_i}{(H/P)_n-(H/P)_0}$ (blue line), slope = 1.00, where P is total pressure in atm, including seawater vapor pressure plus $P(CO_2)$ (cf. Equation (7): $y_i/x_i = H_i/P$).

3.4. The Null Hypothesis, SST, and Cenozoic CO_2

Under the Null Hypothesis, SST drives any increase or decrease in $P(CO_2)$ when $(CO_2)_{total}$ is constant. The entire change in $P(CO_2)$ across the Cenozoic, $\Delta P^{total}_{CO_2}$, is then a function of H_S. If the trans-Cenozoic $\Delta P^{total}_{CO_2}$ is known, then the trend of $P(CO_2)$ will follow the fractional change in H_S. In that light, Equation (10) can be used to calculate $P(CO_2)$ at each point "i" across the Cenozoic.

$$\frac{H_0 - H_i}{H_0 - H_n} \times \Delta P^{total}_{CO_2} = \Delta P(CO_2)_i \quad (10)$$

Estimated in this way, calculated $P(CO_2)$ will vary with SST in the proportion determined by the fractional change in the Henry's Law constant (Equation (10)), within the bounds set by the upper and lower limits of the proxy Cenozoic $P(CO_2)$ trend.

If Cenozoic $[CO_2]_{ocean}$ is constant, the estimated trend in $P(CO_2)$ will strictly vary with SST alone. Alternatively, if the trend in Cenozoic $P(CO_2)$ departs from the Henry's Law trend reflecting a constant $[CO_2]_{ocean}$, then a $\Delta[CO_2]_{ocean}$ is indicated. In this case, the Cenozoic $\Delta P^{total}_{CO_2}$ will vary away from the limit of $\Delta P(CO_2)$ allowed by the range of H_S and SST. The Null Hypothesis Henry's Law $P(CO_2)$ trend will then reflect the disparate partial pressure of CO_2 produced by the apparent $\Delta[CO_2]_{ocean}$ under conditions of the given SST.

This construct constitutes the Null Hypothesis. That SST alone determines the baseline of $P(CO_2)$ across the Cenozoic Period. However, both $[CO_2]_{ocean}$ and SST can vary with geological-scale events, such as carbonate drawdown, volcanic CO_2 outgassing, and ocean warming. When geological-scale perturbations are absent, $P(CO_2)$ varies in proportion to Henry's Law. When they are present, $P(CO_2)$ will depart from the unperturbed Henry's Law trend. Such departures, if present, become visible by comparison with an independent empirical proxy estimate of $P(CO_2)$. The Null Hypothesis includes the significant precept that, all else being equal, changes in SST are precursory to changes in $P(CO_2)$. The role of carbon dioxide radiative forcing is assumed to be negligible or absent.

The efficacy of the Null Hypothesis as a candidate explanation, namely precursory SST and the Henry's Law trend in $P(CO_2)$ calculated using Equation (10), can be tested by comparison with the proxy reconstruction of Cenozoic $P(CO_2)$, which is discussed below.

3.5. Basaltic Flood Magmatism and Ocean Heating

Prior to a comparative test, however, the precursory appearance of elevated SST requires a mechanism. Suggested here is that the magmatism associated with Large Igneous Provinces (LIPs) provided the causal thermal energy. LIPs include enormous outpourings of basaltic magmas, leaving up to millions of cubic km of flood basalts and undersea crustal plateaus [64–67].

The North Atlantic Igneous Province (NAIP), formed during the breakup of Greenland and Eurasia, beginning at 66 MYr BP, includes basaltic extrusions occupying about 1.6×10^6 km^2 of the North Atlantic seafloor [68–70]. The initial magmatic phase of the breakup, ca. 62 MYr BP, produced about 1.8 million km^3 of flood basalts. The later phase, initiating at about 56 MYr BP, coincided with the PETM. Extending over 3–4 Ma, the PETM magmatism produced about 4.5 million km^3 of new marine basaltic crust [67,68,71,72]. The entire NAIP includes about 8.78×10^6 km^3 of flood basalts, of which about 3.35×10^6 km^3 is oceanic [71].

It is here proposed that the elevated SST of the PETM was caused by thermal contact with NAIP magma. A thorough exploration of this hypothesis is well beyond the scope of this work. However, the thermal impact of NAIP magmatism can be illustrated with a zeroth order heat capacity estimate. For this estimate, the heat of fusion of basalt is first combined with the heat capacity of seawater to estimate the ΔT_{ocean} from transmission of the heat of fusion of 1×10^6 km^3 of basaltic magma.

The heat of fusion of basalt is 161.5 cal/g = 675.4 J/g, while the heat capacity for seawater is 3.9912 J g^{-1} K^{-1} (at 15 °C) [73,74]. The world ocean is 1.338×10^9 km^3, of

3.7 km mean depth and 1,036 kg/m^3 mean density [56,75]. The mass of the world ocean is then

$$1.036 \times 10^{12} \text{ kg/km}^3 \times 1.338 \times 10^9 \text{ km}^3 = 1.386 \times 10^{21} \text{ kg}. \quad (11)$$

The density of both basaltic magma and the crystallized solid is set at 2.7 g/cc [76]. The mass of 1×10^6 km^3 of basaltic magma of density 2.7×10^{12} kg/km^3 is then 2.7×10^{18} kg.

The fusion of 2.7×10^{18} kg of basaltic magma produces 1.82×10^{24} J, which is the thermal energy produced during the basaltic phase change of fluid to solid, alone, at constant temperature.

The ΔT of the world ocean from the fluid to solid transition of each one million km^3 of LIP basaltic magma is then estimated as

$$(1.82 \times 10^{24} \text{ J})/(3.9912 \times 10^3 \text{ J kg}^{-1} \text{ K}^{-1} \times 1.386 \times 10^{21} \text{ kg}) = 0.33 \text{ K}. \quad (12)$$

If the thermal plume rises and stratifies in the top 1 km of the ocean (0.27 of ocean volume), then the estimated global $\Delta T_{1km} = 1.2$ K.

This increase in temperature is from the basaltic heat of fusion alone. The temperature of emergent mid-ocean ridge magmas is about 1620 K, while crystallization commences at about 1470 K [76,77]. A complete inventory of the thermal impact of magma should include both the liberated heat of fusion as well as the cooling of the 1620 K molten magma, and the hot solid basalt from 1470 K to ambient sea water temperature.

The heat capacity of solid basalt is non-linear with temperature [78]. The median heat capacity of basalt cooling from 1620–300 K can be estimated as 0.9970 J g^{-1} K^{-1} from the thermochemical work of Richet et al. [78]. The cooling of 1 million km^3 of hot molten basalt from 1620 K through 1470 K to ambient (300 K) yields an estimated

$$\Delta T_{ocean} = (1320 \text{ K} \times 997.0 \text{ J kg}^{-1} \text{ K}^{-1} \times 2.7 \times 10^{18} \text{ kg})/(1.386 \times 10^{21} \text{ kg} \times 3991.2 \text{ J kg}^{-1} \text{ K}^{-1}) = 0.64 \text{ K}. \quad (13)$$

Thus, the total ΔT_{ocean} warming from eruption of 1 million km^3 of 1620 K basaltic magma is 0.97 K, which includes the heat of crystallization at 1470 K plus the heat liberated by cooling from 1620 K.

If the heated sea water plume stratifies in the top 1 km of the ocean, $\Delta T_{1km} = 3.6$ K. With reference to scale, the entire oceanic regions of the NAIP include 3.85 million km^3 of basalt.

Although the present exercise is zeroth order, as noted, it is nevertheless sufficient to establish that the heat produced by the multi-million km^3 of the NAIP oceanic magmatic extrusions may have profoundly increased global SST. This finding provides the required mechanism for the precursory SST of the Null Hypothesis.

3.6. The Null Hypothesis and Trends in Cenozoic P(CO_2)

Turning now to Cenozoic CO_2, a worthwhile estimate of the P(CO_2) trend across the preceding 66 million years has been derived using phytoplankton alkenone and borate δ^{11}B marine proxies [2], discussed more fully in the following section.

This proxy trend provides the independent empirical reference against which to test the Null Hypothesis trend. The degree to which the fractional Henry's Law trend in P(CO_2) (Equation (10)) reproduces the empirical proxy trend will corroborate or invalidate the Null Hypothesis.

The proxy estimate yielded mean $P(CO_2)_n = 1093 \pm 405$ ppm at 65–66 Myr BP [2]. The mean of Pleistocene carbon dioxide used to provide $P(CO_2)_0$, the recent terminus of Cenozoic PCO_2), was taken from the Antarctic ice core EPICA Dome C, wherein mean $P(CO_2)_0 = 231 \pm 28$ ppm over 800 ka of the Pleistocene [51].

The total change in CO_2 (ppm) across the Cenozoic is then, $\Delta P^{total}_{CO_2} = 1093 - 231 = 862$ ppm. From Equation (10), the SST-driven trend in atmospheric CO_2 (ppm) over the 66 Ma of the Cenozoic can be calculated as follows:

$$\text{Cenozoic } CO_2 \text{ (ppm)} = \frac{H_0 - H_i}{H_0 - H_n} \times \Delta P^{total}_{CO_2} + 231 \quad (14)$$

Figure 3 shows the result of this calculation.

The evolution of $P(CO_2)$ over the entire Cenozoic, Figure 3, faithfully reflects the Cenozoic SSTs (cf. Figure 1). The calculated trend in tropospheric CO_2 is constrained to be within the $\Delta P^{total}_{CO_2}$ of the empirical Cenozoic proxy. Thus, although the proxy provides the magnitude of the Cenozoic variation in $P(CO_2)$, it does not reveal the physical cause. Nevertheless, the physical cause of $P(CO_2)$ must include the natural variation in sea surface temperature.

In Figure 3, the zero intercept of the $P(CO_2)$ Lowess smooth is 175 ppm, which represents the mean partial pressure of CO_2 during the glacial Pleistocene. The precipitous decline in CO_2 ppm after about 3 MYr BP reflects, in part, the increasing solubility of carbon dioxide consequent to the rapid decline in SST.

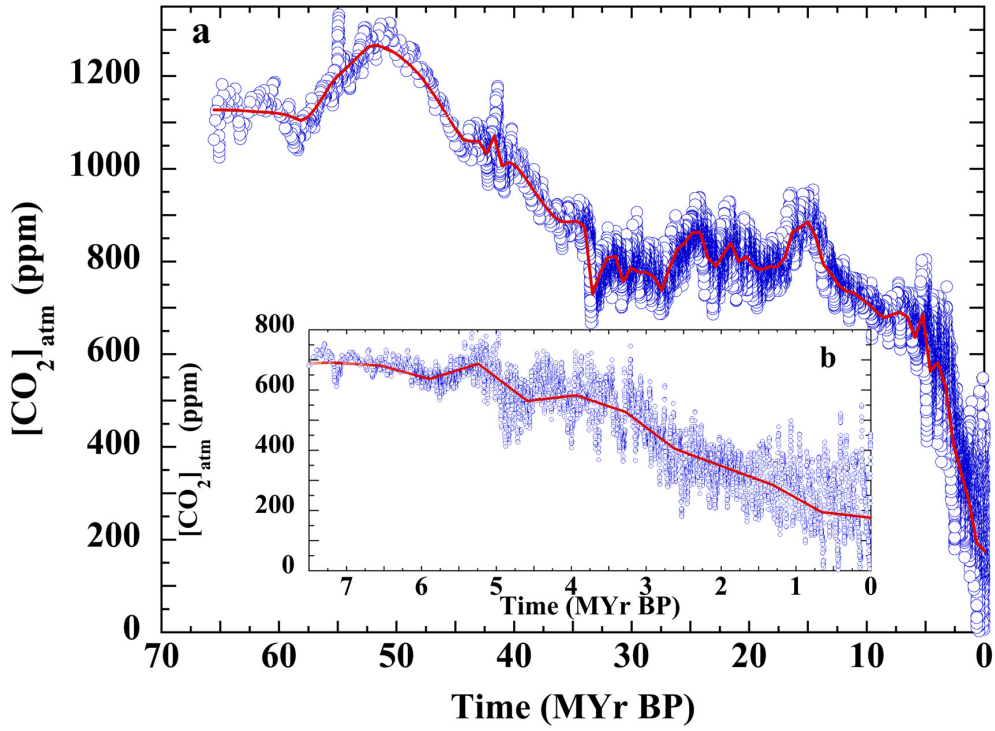


Figure 3. (**a**) (Blue points), $P(CO_2)$ (ppm) as calculated under the Null Hypothesis (Equation (14)), with $\Delta P^{total}_{CO_2}$ = 862 ppm and the fractional ratio of the temperature-varying Henry's Law constant for seawater (Figure 1). The red line is a 1% weighted Lowess smooth. Inset (**b**): expansion of the most recent 7.5 Ma.

However, $P(CO_2)$ is driven by ΔSST alone only when $[CO_2]_{ocean}$ is constant. Cenozoic $[CO_2]_{ocean}$ is known to have decreased following the Eocene, which in turn will have reduced $P(CO_2)$ [2,19,21,28]. A decrease in Cenozoic $[CO_2]_{ocean}$, and thus in $P(CO_2)$, will reduce the value of $\Delta P^{total}_{CO_2}$. In that event, the Null Hypothesis trend (Figure 3) will deviate from the trend of $P(CO_2)$ when driven only by ΔSST. This outcome is illustrated next.

The trend of Cenozoic $P(CO_2)$ reflecting constant $[CO_2]_{ocean}$ can be estimated. Henry's Law was used to calculate the mean initial $[CO_2]_{ocean}$ of the Cenozoic. At the opening of the Cenozoic, the proxy values are mean $P(CO_2) \approx 1100$ ppm and SST = 296.4 K such that the 66 MYr BP $[CO_2]_{ocean}$ can be calculated from Equation (15):

$$\left[CO_2\right]^{66MYrBP}_{ocean} = \left(1.1 \times 10^3 \text{ atm}\right) \times (0.031002 \text{ M/atm}) = 3.41 \times 10^5 \text{ M}. \quad (15)$$

where H_S = 0.031002 M/atm at SST = 296.4 K.

The trend in $P(CO_2)$ resulting from a constant $[CO_2]_{ocean} = 3.41 \times 10^{-5}$ M is shown in Figure 4. Comparison is made with the trend calculated from the Null Hypothesis and the proxy $\Delta P^{total}_{CO_2}$ (cf. Figure 3 and Equation (14)).

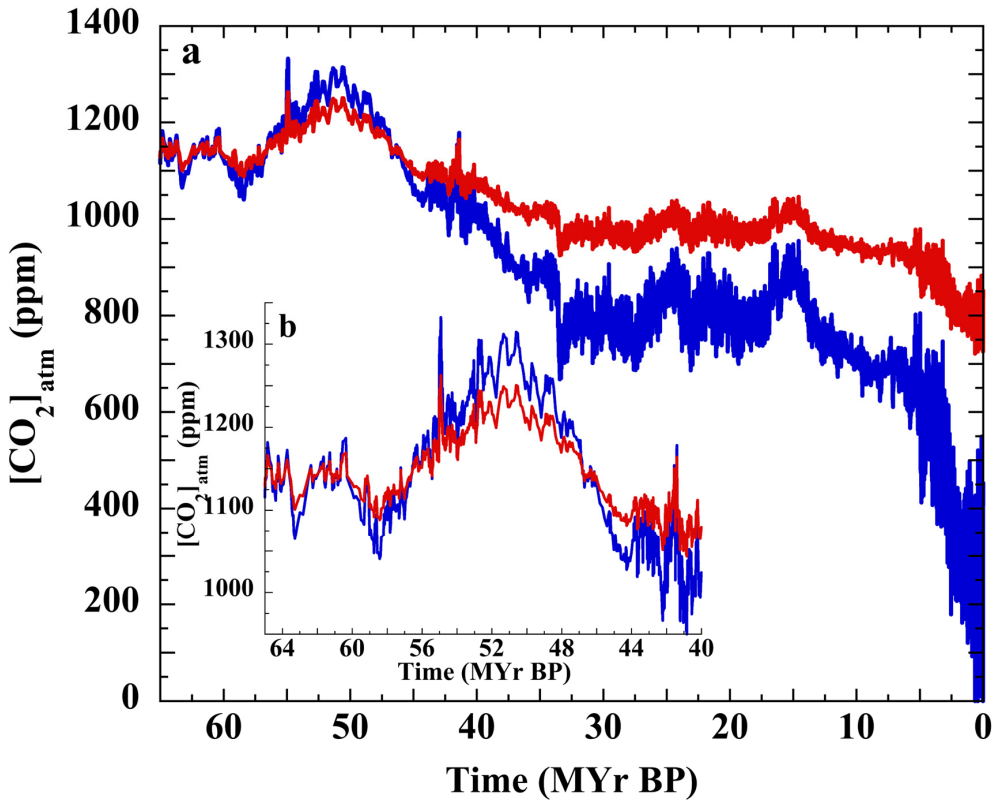


Figure 4. (**a**) (Red line), Henry's Law estimate of the evolution of atmospheric $P(CO_2)$ with varying SST and $[CO_2]_{ocean}$ held constant at the initial Cenozoic concentration of 3.41×10^{-5} M; (blue line), Null Hypothesis estimate of the trend of $P(CO_2)$ constrained to the net proxy Cenozoic $\Delta P^{total}_{CO_2}$ = 862 ppm. Inset (**b**): expansion of the first 25 Ma of the Cenozoic.

Inspection of Figure 4 reveals that the constant $[CO_2]_{ocean}$ and Null Hypothesis trends are very similar over the first 25 Ma of the Cenozoic. Following about 45 MYr BP, the Null Hypothesis $P(CO_2)$ trend traverses a net decline of 900 ppm, diminishing to about 200 ppm at the end of the Pleistocene.

At constant $[CO_2]_{ocean}$, the $P(CO_2)$ declines only to 850 ppm at the end of the Pleistocene, and $\Delta P^{total}_{CO_2}$ = (1093 − 850) ppm = 243 ppm. The much larger proxy $\Delta P^{total}_{CO_2}$ = 862 ppm thus indicates a much greater drop in Cenozoic $P(CO_2)$ than can be accounted by ΔSST alone.

In this regard, had the initial Cenozoic $[CO_2]_{ocean} = 3.41 \times 10^{-5}$ M been maintained, and given the modern Holocene mean SST (292 K), then the preindustrial level of atmospheric carbon dioxide would have been 965 ppm, some 3.3× the observed level. By the same token, the modern SST and the observed pre-industrial $P(CO_2)$ (295 ppm) imply a contemporaneous $[CO_2]_{ocean} = 1.04 \times 10^{-5}$ M.

Thus, the Cenozoic saw a 3.3-fold drop in $[CO_2]_{ocean}$, from 3.41×10^{-5} M to 1.04×10^{-5} M. This large-scale decrease in $[CO_2]_{ocean}$ reiterates the known massive 35-million-year drawdown of marine carbonate since the Eocene.

In this light, the strong decline in $P(CO_2)$ across the Cenozoic may be accounted as a decreasing SST concomitant with large-scale long-term drawdown of dissolved carbonate. These considerations are addressed further below.

3.7. Testing the Null Hypothesis: Atmospheric CO_2 over the Cenozoic

Phytoplankton alkenones and the fractionation of boron isotopes, $\delta^{11}B$, from benthic marine cores have received considerable attention in development of proxies for the level of atmospheric CO_2 [1,14,39,79–91]. These proxies were recently combined to produce a time series of atmospheric CO_2 (ppm) over the full 66 Ma of the Cenozoic [2]. In Figure 5, this

Cenozoic proxy CO_2 time series is compared with the $\Delta P(CO_2)$ trend of the Null Hypothesis, reflecting the $\delta^{18}O$ proxy SST estimate of Hansen et al. (Figure 3, Equation (14)) [33].

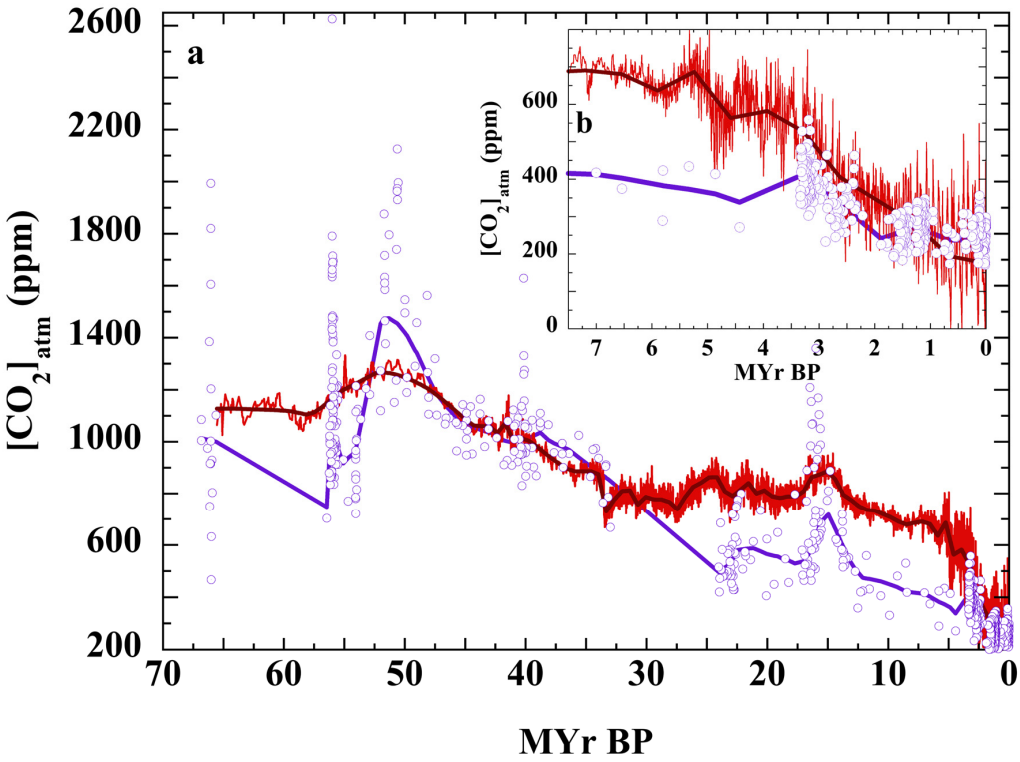


Figure 5. (**a**) (Red line), Null Hypothesis estimate of the trend in atmospheric CO_2 during the Cenozoic; (black line), a 1% weighted Lowess smooth of the estimate; (blue points), Cenozoic $P(CO_2)$ as estimated using marine core alkenone and boron isotope proxies [2]; and (blue line), a 5% weighted Lowess smooth of the proxy-derived trend in Cenozoic $P(CO_2)$. Inset (**b**): expansion of the most recent 7.5 Ma.

Figure 5 reveals that the Null Hypothesis $\Delta P(CO_2)$ estimate of Cenozoic CO_2 traverses through the proxy points across the first 30 million years of the Paleogene, extending from the Paleocene (66–56 MYr BP) through the Eocene (56–34 MYr BP) [92]. The two series diverge at the apparent sharp drop in proxy $P(CO_2)$ between 34 and 23 MYr BP, across the Eocene–Oligocene boundary, with a continuous and nearly constant offset across the Miocene and Pliocene. The two series converge again at about 3 MYr BP, near the Pliocene–Pleistocene boundary.

The Lowess smooth of the Null Hypothesis trend reaches 175 ppm at the Holocene intercept, while that of the proxy series reaches 237 ppm. Over the entire 20 ka of the most recent post-glacial and Holocene, the $P(CO_2)$ means are 269 ± 180 and 278 ± 13 ppm (1σ), respectively. Thus, although the two constructions yield statistically indistinguishable recent $P(CO_2)$, the Null Hypothesis estimate contains the noise of the temperature reconstruction.

Comparison of Figure 5 with Figure 4 shows the trend reflecting constant $[CO_2]_{ocean}$ (3.41×10^{-5} M) departs much more strongly from the proxy trend Lowess smooth after 33 Ma BP, and does not parallel the declining slope at all (the comparison of the proxy trend with the evolution of Cenozoic $P(CO_2)$ with constant 3.41×10^{-5} M $[CO_2]_{ocean}$ is shown in Figure S1 of the Supporting Information).

3.8. The PETM and Cenozoic $P(CO_2)$

Bijl and associates have derived an alternative proxy sea surface temperature series extending over the Paleocene and Eocene epochs [60,93]. The proxies included alkenones and archaea GDGT membrane lipids [94], extracted from benthic sedimentary cores recovered from the South Pacific. The derived trend of South Pacific proxy SSTs correlated

extremely well with the global trend of foraminiferal proxies, and therefore was assessed to have global significance.

Figure 6a shows the proxy SSTs of Bijl, et al. A maximum of about 35 °C is reached at 55 MYr BP, some 7 °C higher than the reconstruction of Hansen et al. [33]. However, the alternative reconstructions are of similar intensities at the early Paleocene, 66 MYr BP, and merge again after 40 MYr BP (Figure 6a). This coalescence permits appending the two proxies at 40 MYr BP, which allows using Equation (14) to reconstruct the full Cenozoic trend of atmospheric CO_2 under the PETM implied by the SST of Bijl et al. [60].

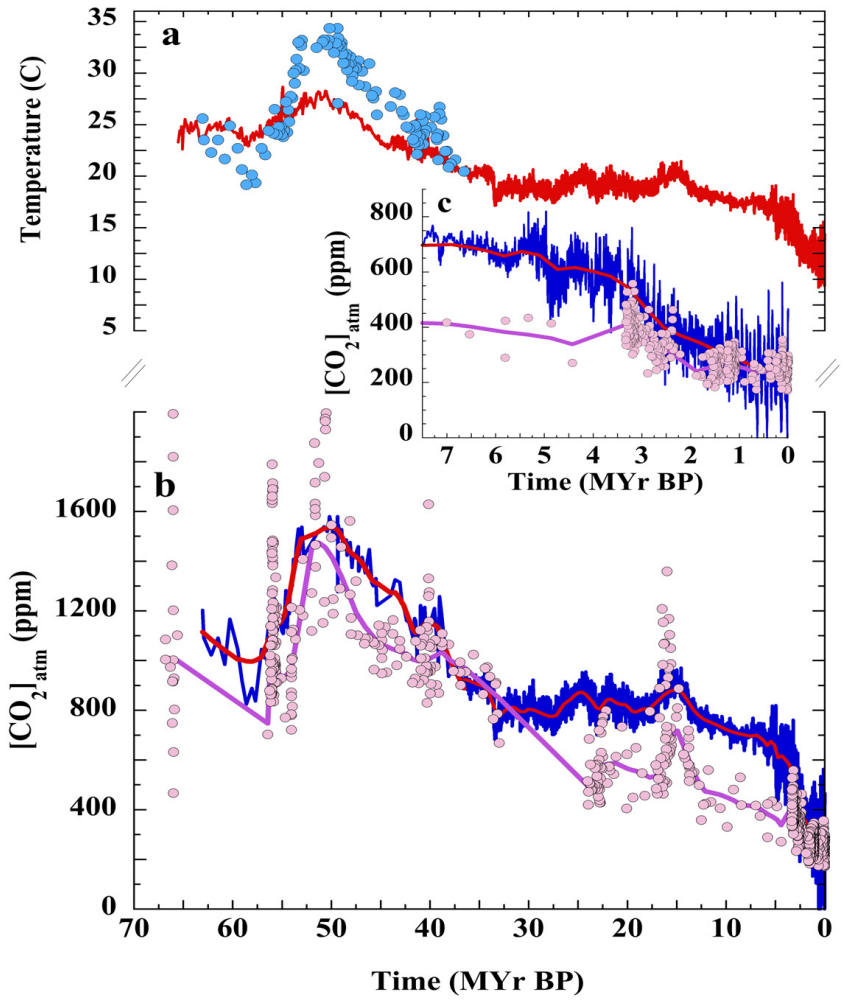


Figure 6. (**a**) (Blue points), the Paleocene–Eocene proxy SST reconstruction of Bijl et al. (2009) [60]; (red line), the Hansen et al. (2013) proxy SST reconstruction [33]. The two reconstructions merge across 40 to 37 MYr BP. (**b**) (Pink points), proxy P(CO_2) reconstruction of Rae et al. (2021), using marine core alkenone and boron isotope proxies [2]; (purple line), 5% weighted Lowess fit through the points of the proxy; (blue line), estimate of Cenozoic P(CO_2) (ppm) calculated using Equation (14), including the PETM SSTs of Bijl et al. [60]; and (red line), piece-wise weighted Lowess fit to the Cenozoic CO_2 estimate. The weights were 15% over the reconstruction of Bijl et al., (65–37 MYr BP) [60], and 1% over 37–0 MYr BP. Inset (**c**): expansion of the most recent 7.5 Ma.

To accomplish this reconstruction, a new h_G was calculated over the Cenozoic proxy SST trend (Equation (4)) that included the Bijl et al., PETM sea surface temperatures [60]. Equations (2), (3) and (5) were then used to calculate a new series of Cenozoic $H_{seawater}$. Figure 6b,c show the new Null Hypothesis estimate of Cenozoic P(CO_2) using the Bijl et al., PETM SSTs [60]. The P(CO_2) estimated from marine core proxies is again included for comparison [2].

Figure 6b shows that the Null Hypothesis reconstruction using the Bijl et al., SSTs is more consistent with the proxy-derived PETM maximum $P(CO_2)$ than the reconstruction using the $\delta^{18}O$ proxy SST reconstruction (compare Figure 5) [33,60]. The consistency persists through the early Eocene to ca. 50 MYr BP. However, a divergence appears at 47 to 41 MYr BP as the PETM maximum cooled during the Eocene. Correspondence with the proxy record re-emerges near 40 MYr BP, and this continues for a further 8 Ma. The previously observed $P(CO_2)$ offset repeats after the mid-Oligocene, about 32 MYr BP, and through Miocene and Pliocene until the Pleistocene (*cf.* also Figure 5).

4. Discussion

4.1. The Null Hypothesis

Cenozoic $P(CO_2)$ has been estimated within the Null Hypothesis proposition that SST drove the baseline level of atmospheric CO_2. The Null Hypothesis trend is very consistent with the trend derived from CO_2 proxies over the first 30 Ma of the Cenozoic, and the final 3 Ma. Across 30 MYr BP to 3 MYr BP, the proxy trend is offset about 300 ppm below the Null Hypothesis trend.

When $[CO_2]_{ocean}$ is modified by geological-scale perturbations, then the Null formalism (Equation (14)) trend will depart from the $P(CO_2)$ determined by SST alone. The greater intensity of the points of the proxy reconstruction over Null Hypothesis $P(CO_2)$ at the PETM around 52 MYr BP is suggestive that the elevated $P(CO_2)$ during the PETM was not solely a product of the greater SST, but included CO_2 outgassing during the NAIP magmatism. Thus, the Henry's Law deduction provides a baseline reference that can reveal the presence and impact of external physical processes affecting $P(CO_2)$. These are discussed next.

4.2. The Paleocene–Eocene Thermal Maximum (PETM)

Overall, the SST reconstruction of Bijl et al. (2009) more closely reproduces the PETM $P(CO_2)$ maximum [60]. The Henry's Law $P(CO_2)$ trend closely tracks the proxy trend across 30 million years of the Paleocene and Eocene, as well as across the Pleistocene (Figures 5 and 6). Reduction of CO_2 solubility in a warmer ocean is responsible for much of the enhanced $P(CO_2)$ during the PETM, 56–52 MYr BP, as well as the greater $P(CO_2)$ of the late-Oligocene/early-Miocene warm period (22 MYr BP), and during the Miocene Climatic Optimum (MCO, 15 MYr BP). These correspondences imply that SST alone governed $P(CO_2)$ almost exclusively over extensive portions of the Paleogene. Absent of large-scale perturbations, SST governance of $P(CO_2)$ would have persisted over the whole of the 66 Ma Cenozoic.

Justification of the 49 to 41 MYr BP negative divergence as physically real requires evidence of contemporaneous CO_2 drawdown processes. Indeed, evidence of a general drawdown of CO_2 following the PETM maximum has been found in geological indicators of enhanced chemical weathering, high coccolithophore productivity, and a rapid expansion of photosynthetic sequestration with increased deposition of organic matter [13,15,20,26–28,30,95–100].

The second major divergence emerged at 32 MYr BP, near the Eocene–Oligocene boundary. The drop of $P(CO_2)$ across the Miocene, with the exception of the 15 MYr BP pulse associated with the MCO, is well known and well characterized as changes in ocean circulation, orbital forcing, increased chemical weathering, e.g., from surfaces emergent during the Himalayan uplift, the impact of sea-level fall on carbonate deposition, and the initiation of the Antarctic Circumpolar Current [1–4,7,9,14,25,39,86,101–104]. The various perspectives on geological mechanisms driving $P(CO_2)$ during the Paleocene have been reviewed [1,2,5,22,24,105,106]. These remain subjects of considerable discussion but are beyond the scope of this work.

4.3. The Miocene Climate Optimum

The Miocene excursion in $P(CO_2)$ (17 to 13 MYr BP) tracks the MCO warm pulse in SST, which in turn coincides with the Monterey $\delta^{13}C$ excursion, indicating a large-scale modification of the marine carbon cycle [3,101]. Moreover, Figure 7 shows that the overall spike in $P(CO_2)$ appears to have exceeded the increase induced by higher SST alone.

In Figure 7, the ordinate ranges are identical, with the baseline trends offset into coincidence. This allows a direct comparison of the slopes and intensities of the smoothed proxy and the Null Hypothesis estimate. The proxy baseline both enters and exits the Miocene $P(CO_2)$ pulse signal completely coincident with the Null Hypothesis trend, indicating the same background slope despite the offset (cf. Figure 6). The respective 15 MYr BP $P(CO_2)$ spikes are coincident.

The nominally greater intensity of the MCO proxy $P(CO_2)$ signal is suggestive that CO_2 entered the atmosphere during the Miocene Burdigalian–Langhian stages in excess over that released by the warm SST re-equilibration alone. Uncertainties are not included in Figure 7, but resolution alone does not allow a clear distinction in timing or intensity between the two spikes [2,33]. Nevertheless, a large fraction of the rise in $P(CO_2)$ during the MCO can be explained as a direct physico-chemical response to a general increase in SST, namely gas-solute re-equilibration following a warmed global ocean. The mid-Miocene Columbia River volcanism (ca 17 to 15 MYr BP) coincides very well with the opening stages of the MCO pulse and is thus a strong candidate source of increased $[CO_2]_{ocean}$ and increased SST [11,101].

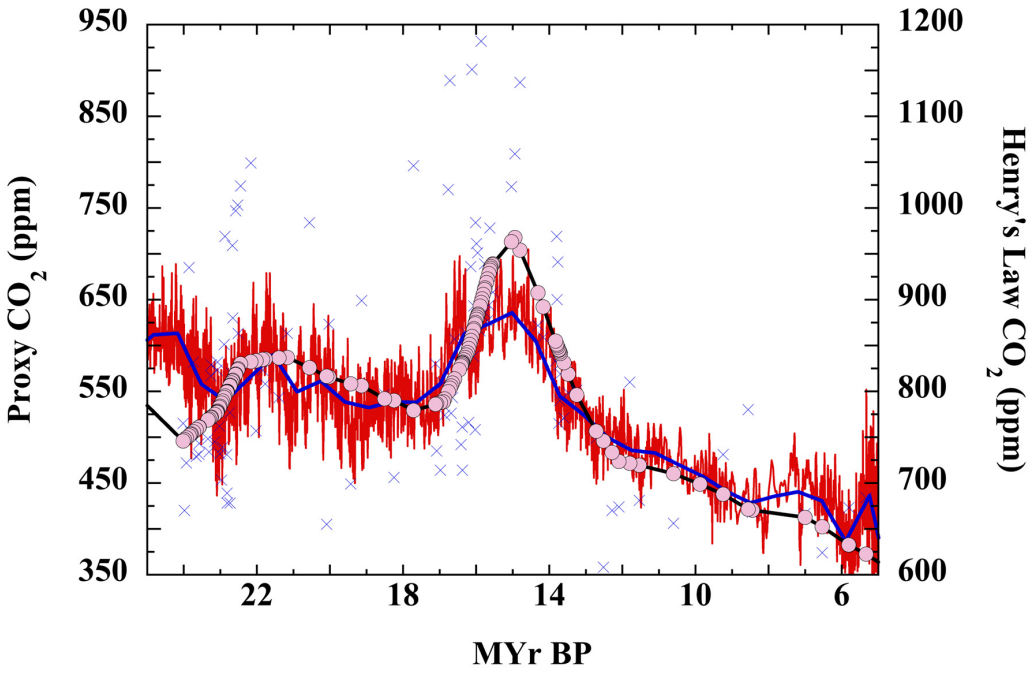


Figure 7. Double-y plot of the increase in $P(CO_2)$ during the MCO. (× points), proxy $P(CO_2)$ trend across the MCO [2]; (circular points plus black line), the proxy $P(CO_2)$ trend and the Lowess smooth (cf. Figures 4 and 5); (red line), the Null Hypothesis estimate of SST-limited $P(CO_2)$ (cf. Figure 3); and (blue line), the Lowess smooth of the Null Hypothesis estimate. Both ordinates include a 550-ppm range but have been vertically offset so as to bring the two background slopes into coincidence.

4.4. Pleistocene and Holocene

The proxy $P(CO_2)$ trend and the Null Hypothesis estimate come into coincidence again at and across the Pleistocene (cf. Figures 5 and 6). At 3 MYr BP, $[CO_2]_{ocean} = 1.50 \times 10^{-5}$ M is calculated from the proxy mean $P(CO_2)$ of 380 ppm and the value of H_S at the SST proxy mean is 288 K. At 1 MYr BP, $[CO_2]_{ocean} = 1.15 \times 10^{-5}$ M is calculated for the mean proxy SST = 286 K and the mean $P(CO_2)$ proxy = 272 ppm. These considerations are

suggestive that a three-million-year decline in $P(CO_2)$ was driven both by decreasing SST and a significant carbonate drawdown. Figure S5 of the Supporting Information shows the decline in $[CO_2]_{ocean}$ across the Cenozoic consequent to the proposed drawdown of carbonate. The decrease in $[CO_2]_{ocean}$ is unlikely the result of a global increase in seawater pH (cf. Figure S6 and discussion in the Supporting Information) [107].

In the late Pleistocene, the rises and falls of SST and atmospheric CO_2 are coincident with retreats and advances of glaciation. A direct Henry's Law calculation of $P(CO_2)$ was carried out to test whether the Cenozoic $\delta^{18}O$ proxy SST record can explain the 420 ka of $\Delta P(CO_2)$ recovered from the VOSTOK ice core [33].

The $[CO_2]_{ocean}$ of the late Pleistocene gas-solute equilibrium reservoir was calculated as follows:

$$[CO_2]_{ocean} = 285 \times 10^{-6} \text{ atm} \times 0.035018 \text{ M/atm.} = 9.980 \times 10^{-6} \text{ M}, \quad (16)$$

where 285×10^{-6} atm is the pre-industrial $P(CO_2)$ obtained from the West Antarctic Ice Sheet (WAIS) ice core [108], and the second term is the Henry's Law constant for seawater at 292.05 K (18.9 °C), the ERSST v5 1960–1990 global mean ocean SST. The $[CO_2]_{ocean}$ was assumed to be invariant over the past 500 ka (cf. Figure S5 inset b of the Supporting Information). In comparison, the current oceanic mean of molecular $[CO_2]_{ocean}$, including at depth, is 1.005×10^{-5} M [56].

The 420 ka trend in $P(CO_2)$ was calculated as follows:

$$P(CO_2) = [CO_2]_{ocean} \text{ (M)} \times H_S \text{ (atm/M)} \quad (17)$$

where H_S tracks the variation in $\delta^{18}O$ proxy SST over the 420 ka of the glacial–interglacial period. However, Figure S2 of the Supporting Information shows the calculated $P(CO_2)$ trend to be vertically offset and compressed relative to the $P(CO_2)$ trend recovered from the VOSTOK ice core.

The problem with reproducing the VOSTOK $P(CO_2)$ must reside in H_S. The top 400 m of the ocean, where CO_2 is present as the dissolved molecule [109], presently contains about 3.4 times more carbon dioxide than the atmosphere. Thus, $P(CO_2)$ swings caused by SST can occur without a significant change in $[CO_2]_{ocean}$ (dissolved molecular CO_2 is in equilibrium with the much larger concentrations of dissolved carbonate). The discrepancy must then derive from the $\delta^{18}O$ proxy SST, which plays a direct role in determining H_S (Equation (4)).

Proxies have been interpreted to indicate a ~4 °C range of glacial–interglacial SST [33,110,111]. However, this SST range could not replicate the glacial–interglacial shifts in $P(CO_2)$ indicated by the VOSTOK ice core data. The replication problem was resolved when the range of glacial–interglacial SST was expanded to about 11 °C (280–291 K) (Figure S3 of the Supporting Information). The expanded range of SSTs were then used to generate a revised set of H_S constants, shown in Figure 8a.

The 420 ka trend in $P(CO_2)$ was then re-calculated using the revised Henry's Law constants and $[CO_2]_{ocean} = 9.980 \times 10^{-6}$ M (Equation (17)). Figure 8b shows the recalculated $P(CO_2)$ trend, which is a close match to the $P(CO_2)$ record of bubble-trapped gas from the VOSTOK ice core.

For comparison, the VOSTOK $P(CO_2)$ was also calculated within the Null Hypothesis (Equation (18)):

$$P(CO_2) = \frac{H_0 - H_i}{H_0 - H_n} \times \Delta P_{CO_2}^{total} + 182.5, \quad (18)$$

where H_0 and H_n retain their previous meaning, $\Delta P_{CO_2}^{total} = 116.5$ ppm (the VOSTOK range) and 182.5 ppm is the VOSTOK minimum.

Figure 8c compares the $P(CO_2)$ trends calculated directly from Henry's Law (Equation (17)) and from the Null Hypothesis (Equation (18)).

The revised Henry's Law $P(CO_2)$ trend, Figure 8b, captures the main elements of the VOSTOK ice core CO_2 record. Temperature-driven re-equilibration of carbon dioxide across

the sea surface can explain the rise and fall of atmospheric $P(CO_2)$ throughout the 420 kYr glacial record of the VOSTOK ice core. The correspondence implies a glacial–interglacial global mean SST range of 11 °C (280–291 K), which is very close to the estimated 11.3 °C West Antarctic air temperature transition from the Last Glacial Maximum (LGM) to the Holocene [112].

The revised Henry's Law estimate for Holocene $P(CO_2)$ is 280 ppm, very close to the pre-industrial value. Likewise, the revised Holocene SST is 291 K, very close to the present global mean (Figure S3 in the Supporting Information). The correspondence with the direct Henry's Law calculation substantiates the Null Hypothesis methodology.

Importantly, the needed revision of the end-Pleistocene $\delta^{18}O$ SSTs is suggestive of a need to re-examine the Cenozoic $\delta^{18}O$ proxy SST record itself. It seems possible that the 66 Ma record of SST may have varied with greater intensity than presently indicated.

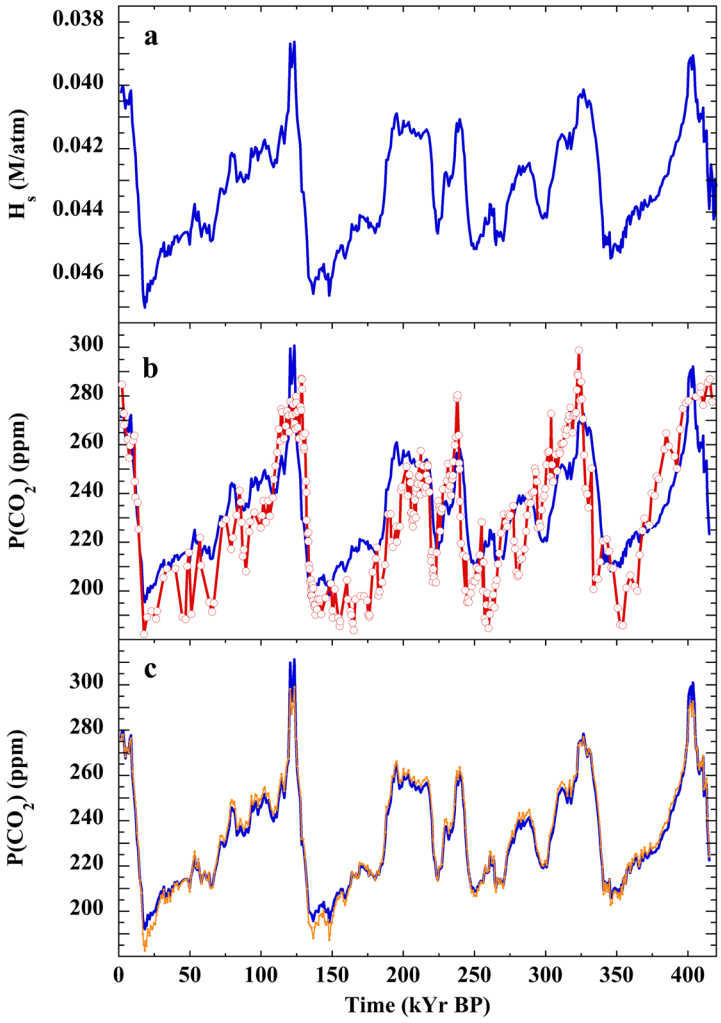


Figure 8. (**a**) Henry's Law constants for seawater reflecting the adjusted SSTs (see text). Note the descending ordinate. (**b**) (Red line plus points), VOSTOK ice core $P(CO_2)$ record; and (blue line), $P(CO_2)$ calculated using $[CO_2]_{ocean} = 9.980 \times 10^{-6}$ M and the adjusted H_S reflecting an 11 °C glacial/interglacial temperature range (Equation (17)). (**c**) Method comparison: (blue line), replication of the VOSTOK $P(CO_2)$ calculated using the adjusted Henry's Law constants (Equation (17)); and (orange line), VOSTOK $P(CO_2)$ calculated according to the Null Hypothesis using the ratio of adjusted H_S values and the VOSTOK $\Delta P^{total}_{CO_2}$ (Equation (18)). The two estimates express the assumption that the rises and falls of glacial/interglacial atmospheric $P(CO_2)$ reflect re-equilibrations across the sea surface driven by time-varying SST, alone.

The methodological approach to $P(CO_2)$ developed here would be equally useful to any revised Cenozoic SST record, because any revised Henry's Law constants would faithfully reflect any revised trend in SST.

5. Conclusions

A general conclusion stemming from the sum of results reported here is that the causal direction relating SST and $P(CO_2)$ across the Cenozoic is consistent with SST having driven $P(CO_2)$ rather than the reverse. The success of the Henry's Law reproduction of the VOSTOK $P(CO_2)$ record extends this conclusion through the Pleistocene glaciations and into the Holocene.

Finally, ocean heating from the magmatic extrusions of LIPs may have been responsible for the extended climatic warm periods, most notably entering the PETM and during the MCO [11,68,69,113,114]. In this light, the general decline in SST across the Cenozoic may reflect a relative quiescence of submarine magmatism and thus of magmatic heating, rather than being caused by a secular decline in the radiative forcing of atmospheric CO_2 [115–117]. One notes in passing that extended ocean cooling due to long-term quiescence of submarine magmatism may have initiated snowball Earth events, which were times of low tectonic activity [118–120]. Also, the Pleistocene ice ages began only after the extended cooling period of the Cenozoic ocean. Equivalently large Milankovitch orbital forcing must have been present during the late Cretaceous and throughout the Cenozoic [121–123], but did not produce glaciations.

Other important and long-term impacts include geo- and/or biophysical carbonate drawdowns that strongly reduced $P(CO_2)$, most notably in the cooling phase of the PETM and from the Oligocene through to the Pleistocene. The Henry's Law estimate of $[CO_2]_{ocean}$ indicated that carbonate drawdown continued into the opening of the glacial period, about 700 ka BP (cf. Figure S5 of the Supporting Information, which shows a decline in $[CO_2]_{ocean}$ of about 1.8×10^{-6} M across the most recent 1 MYr BP of the Pleistocene).

Finally, the correspondence of the Null Hypothesis estimates with the proxy $P(CO_2)$ and the Henry's Law reproduction of the VOSTOK record implies that sea surface temperature has been the primary determinant of baseline atmospheric $P(CO_2)$ across the entire Cenozoic. SST-driven means that ambient CO_2 is released or dissolved only after a positive or negative change in global ocean temperature. The correlation of $P(CO_2)$ and surface temperature across geological time then arises from the changing solubility of CO_2 in response to the independent variation in SST. Geological-scale drawdowns of carbonate or releases of CO_2 have significantly modified the record, but these changes are not necessary for a baseline explanation of $P(CO_2)$ or of surface temperature.

That is, the most parsimonious interpretation of the Cenozoic record is that ocean temperature rose with large-scale magmatic activity and fell in its absence. $P(CO_2)$ followed. In this light, atmospheric CO_2 has been a molecular spectator of the changing climate.

Interposition of the radiative forcing of an exogenous increase or decrease of CO_2, which initiates and sustains a change in SST, is superfluous to a straightforward explanation of climate and $P(CO_2)$: warmer/higher during vigorous magmatic periods, and cooler/lower in their absence. The notion of exogenous CO_2 forcing adds no additional explanatory value. Apart from geologically-scaled bio- and/or geophysical events, SST appears to have fully governed atmospheric $P(CO_2)$ across the 66 MYr of the Cenozoic. A generalizing conclusion is that the dogma of atmospheric CO_2 as the predominant driver of global surface temperature should be set aside.

Supplementary Materials: The following supporting information can be downloaded at https://www.mdpi.com/article/10.3390/geosciences14090238/s1, Figure S1: Cenozoic CO_2: comparison of proxy and Henry's Law estimates; Figure S2: Comparison of the 420 ka VOSTOK CO_2 record with a Henry's Law estimate using SSTs from Hansen et al. (2013) [33]; Figure S3: Cosine fit to the 420 ka VOSTOK CO_2 record; Figure S4: Comparison of two Henry's Law estimates of the 420 ka VOSTOK CO_2 record before and after an 11 °C adjustment of SST; Figure S5: Henry's Law reconstruction of $[CO_2]_{ocean}$ across the Cenozoic incorporating the PETM SSTs of Bijl et al. (2008) [60]; Figure S6: The

species distribution with pH of 0.002033 M CO_2 in 0.57 M aqueous NaCl; Table S1: Weights for Least Square Fit of $\Delta H_i/\Delta H_n$ vs. $\Delta P(CO_2)_i/\Delta P(CO_2)_n$; Ascii file: Henry's Law Seawater Hansen SSTs; Ascii file: Henry's Law Seawater Bijl Composite. References [2,33,56,59,60,107,124] are cited in the Supplementary Materials.

Funding: This research received no external funding.

Data Availability Statement: All data are available in the cited sources.

Acknowledgments: This work was carried out on the author's own time, and has no association with the SLAC National Accelerator Laboratory, the Stanford Synchrotron Radiation Lightsource, or with Stanford University. Use of the magnificent library resources of Stanford University is acknowledged with gratitude.

Conflicts of Interest: The author declares no conflicts of interest.

References

1. Pearson, P.N.; Palmer, M.R. Atmospheric carbon dioxide over the past 60 million years. *Nature* **2000**, *406*, 695–699. [CrossRef] [PubMed]
2. Rae, J.W.B.; Zhang, Y.G.; Liu, X.; Foster, G.L.; Stoll, H.M.; Whiteford, R.D. Atmospheric CO_2 over the Past 66 Million Years from Marine Archives. *Annu. Rev. Earth Planet. Sci.* **2021**, *49*, 609–641. [CrossRef]
3. Raitzsch, M.; Bijma, J.; Bickert, T.; Schulz, M.; Holbourn, A.; Kučera, M. Atmospheric carbon dioxide variations across the middle Miocene climate transition. *Clim. Past* **2021**, *17*, 703–719. [CrossRef]
4. Wang, Y.; Momohara, A.; Wang, L.; Lebreton-Anberrée, J.; Zhou, Z. Evolutionary History of Atmospheric CO_2 during the Late Cenozoic from Fossilized Metasequoia Needles. *PLoS ONE* **2015**, *10*, e0130941. [CrossRef] [PubMed]
5. Westerhold, T.; Marwan, N.; Drury, A.J.; Liebrand, D.; Agnini, C.; Anagnostou, E.; Barnet, J.S.K.; Bohaty, S.M.; De Vleeschouwer, D.; Florindo, F.; et al. An astronomically dated record of Earth's climate and its predictability over the last 66 million years. *Science* **2020**, *369*, 1383–1387. [CrossRef]
6. Zachos, J.C.; Dickens, G.R.; Zeebe, R.E. An early Cenozoic perspective on greenhouse warming and carbon-cycle dynamics. *Nature* **2008**, *451*, 279–283. [CrossRef]
7. Zhang, Y.G.; Pagani, M.; Liu, Z.; Bohaty, S.M.; DeConto, R. A 40-million-year history of atmospheric CO_2. *Philos. Trans. R. Soc. A Math. Phys. Eng. Sci.* **2013**, *371*, 20130096. [CrossRef]
8. Royer, D.L. *6.11—Atmospheric CO_2 and O_2 During the Phanerozoic: Tools, Patterns, and Impacts, in Treatise on Geochemistry*, 2nd ed.; Holland, H.D., Turekian, K.K., Eds.; Elsevier: Oxford, UK, 2014; pp. 251–267.
9. Guillermic, M.; Misra, S.; Eagle, R.; Tripati, A. Atmospheric CO_2 estimates for the Miocene to Pleistocene based on foraminiferal δ11B at Ocean Drilling Program Sites 806 and 807 in the Western Equatorial Pacific. *Clim. Past* **2022**, *18*, 183–207. [CrossRef]
10. Herbert, T.D.; Dalton, C.A.; Liu, Z.; Salazar, A.; Si, W.; Wilson, D.S. Tectonic degassing drove global temperature trends since 20 Ma. *Science* **2022**, *377*, 116–119. [CrossRef]
11. Kasbohm, J.; Schoene, B. Rapid eruption of the Columbia River flood basalt and correlation with the mid-Miocene climate optimum. *Sci. Adv.* **2018**, *4*, eaat8223. [CrossRef]
12. Schaller, M.F.; Fung, M.K. The extraterrestrial impact evidence at the Palaeocene–Eocene boundary and sequence of environmental change on the continental shelf. *Philos. Trans. R. Soc. A Math. Phys. Eng. Sci.* **2018**, *376*, 20170081. [CrossRef] [PubMed]
13. Kelly, D.C.; Zachos, J.C.; Bralower, T.J.; Schellenberg, S.A. Enhanced terrestrial weathering/runoff and surface ocean carbonate production during the recovery stages of the Paleocene-Eocene thermal maximum. *Paleoceanography* **2005**, *20*. [CrossRef]
14. Mejía, L.M.; Méndez-Vicente, A.; Abrevaya, L.; Lawrence, K.T.; Ladlow, C.; Bolton, C.; Cacho, I.; Stoll, H. A diatom record of CO2 decline since the late Miocene. *Earth Planet. Sci. Lett.* **2017**, *479*, 18–33. [CrossRef]
15. Stoll, H.M.; Shimizu, N.; Archer, D.; Ziveri, P. Coccolithophore productivity response to greenhouse event of the Paleocene–Eocene Thermal Maximum. *Earth Planet. Sci. Lett.* **2007**, *258*, 192–206. [CrossRef]
16. McKay, D.I.A.; Tyrrell, T.; Wilson, P.A. Global carbon cycle perturbation across the Eocene-Oligocene climate transition. *Paleoceanography* **2016**, *31*, 311–329. [CrossRef]
17. Basak, C.; Martin, E.E. Antarctic weathering and carbonate compensation at the Eocene–Oligocene transition. *Nat. Geosci.* **2013**, *6*, 121–124. [CrossRef]
18. Beerling, D.J.; Taylor, L.L.; Bradshaw, C.D.C.; Lunt, D.J.; Valdes, P.J.; Banwart, S.A.; Pagani, M.; Leake, J.R. Ecosystem CO_2 starvation and terrestrial silicate weathering: Mechanisms and global-scale quantification during the late Miocene. *J. Ecol.* **2012**, *100*, 31–41. [CrossRef]
19. A Bestland, E. Weathering flux and CO2 consumption determined from palaeosol sequences across the Eocene–Oligocene transition. *Palaeogeogr. Palaeoclim. Palaeoecol.* **2000**, *156*, 301–326. [CrossRef]
20. Chen, Z.; Ding, Z.; Yang, S.; Zhang, C.; Wang, X. Increased precipitation and weathering across the Paleocene-Eocene Thermal Maximum in central China. *Geochem. Geophys. Geosystems* **2016**, *17*, 2286–2297. [CrossRef]
21. Dutkiewicz, A.; Müller, R.D.; Cannon, J.; Vaughan, S.; Zahirovic, S. Sequestration and subduction of deep-sea carbonate in the global ocean since the Early Cretaceous. *Geology* **2018**, *47*, 91–94. [CrossRef]

22. Goddéris, Y.; Donnadieu, Y. A sink- or a source-driven carbon cycle at the geological timescale? Relative importance of palaeogeography versus solid Earth degassing rate in the Phanerozoic climatic evolution. *Geol. Mag.* **2019**, *156*, 355–365. [CrossRef]
23. John, C.M.; Banerjee, N.R.; Longstaffe, F.J.; Sica, C.; Law, K.R.; Zachos, J.C. Clay assemblage and oxygen isotopic constraints on the weathering response to the Paleocene-Eocene thermal maximum, east coast of North America. *Geology* **2012**, *40*, 591–594. [CrossRef]
24. Kump, L.R.; Brantley, S.L.; Arthur, M.A. Chemical Weathering, Atmospheric CO_2, and Climate. *Annu. Rev. Earth Planet. Sci.* **2000**, *28*, 611–667. [CrossRef]
25. Passchier, S.; Krissek, L.A. Oligocene–Miocene Antarctic continental weathering record and paleoclimatic implications, Cape Roberts drilling Project, Ross Sea, Antarctica. *Palaeogeogr. Palaeoclimatol. Palaeoecol.* **2008**, *260*, 30–40. [CrossRef]
26. Penman, D.E. Silicate weathering and North Atlantic silica burial during the Paleocene-Eocene Thermal Maximum. *Geology* **2016**, *44*, 731–734. [CrossRef]
27. Penman, D.E.; Turner, S.K.; Sexton, P.F.; Norris, R.D.; Dickson, A.J.; Boulila, S.; Ridgwell, A.; Zeebe, R.E.; Zachos, J.C.; Cameron, A.; et al. An abyssal carbonate compensation depth overshoot in the aftermath of the Palaeocene–Eocene Thermal Maximum. *Nat. Geosci.* **2016**, *9*, 575–580. [CrossRef]
28. Von Strandmann, P.A.E.P.; Jones, M.T.; West, A.J.; Murphy, M.J.; Stokke, E.W.; Tarbuck, G.; Wilson, D.J.; Pearce, C.R.; Schmidt, D.N. Lithium isotope evidence for enhanced weathering and erosion during the Paleocene-Eocene Thermal Maximum. *Sci. Adv.* **2021**, *7*, eabh4224. [CrossRef]
29. Pollard, D.; Kump, L.; Zachos, J. Interactions between carbon dioxide, climate, weathering, and the Antarctic ice sheet in the earliest Oligocene. *Glob. Planet. Chang.* **2013**, *111*, 258–267. [CrossRef]
30. Ramos, E.J.; Breecker, D.O.; Barnes, J.D.; Li, F.; Gingerich, P.D.; Loewy, S.L.; Satkoski, A.M.; Baczynski, A.A.; Wing, S.L.; Miller, N.R.; et al. Swift Weathering Response on Floodplains during the Paleocene-Eocene Thermal Maximum. *Geophys. Res. Lett.* **2022**, *49*, e2021GL097436. [CrossRef]
31. Li, G.; Ji, J.; Chen, J.; Kemp, D.B. Evolution of the Cenozoic carbon cycle: The roles of tectonics and CO_2 fertilization. *Glob. Biogeochem. Cycles* **2009**, *23*, GB1009. [CrossRef]
32. Wallmann, K. Controls on the cretaceous and cenozoic evolution of seawater composition, atmospheric CO_2 and climate. *Geochim. Cosmochim. Acta* **2001**, *65*, 3005–3025. [CrossRef]
33. Hansen, J.; Sato, M.; Russell, G.; Kharecha, P. Climate sensitivity, sea level and atmospheric carbon dioxide. *Philos. Trans. R. Soc. A Math. Phys. Eng. Sci.* **2013**, *371*, 20120294. [CrossRef] [PubMed]
34. E Hansen, J.; Sato, M.; Simons, L.; Nazarenko, L.S.; Sangha, I.; Kharecha, P.; Zachos, J.C.; von Schuckmann, K.; Loeb, N.G.; Osman, M.B.; et al. Global warming in the pipeline. *Oxf. Open Clim. Chang.* **2023**, *3*, kgad008. [CrossRef]
35. Anagnostou, E.; John, E.H.; Edgar, K.M.; Foster, G.L.; Ridgwell, A.; Inglis, G.N.; Pancost, R.D.; Lunt, D.J.; Pearson, P.N. Changing atmospheric CO_2 concentration was the primary driver of early Cenozoic climate. *Nature* **2016**, *533*, 380–384. [CrossRef] [PubMed]
36. Fletcher, B.J.; Brentnall, S.J.; Anderson, C.W.; Berner, R.A.; Beerling, D.J. Atmospheric carbon dioxide linked with Mesozoic and early Cenozoic climate change. *Nat. Geosci.* **2008**, *1*, 43–48. [CrossRef]
37. Glikson, A. Cenozoic mean greenhouse gases and temperature changes with reference to the Anthropocene. *Glob. Change Biol.* **2016**, *22*, 3843–3858. [CrossRef]
38. Royer, D.L.; Pagani, M.; Beerling, D.J. Geobiological constraints on Earth system sensitivity to CO_2 during the Cretaceous and Cenozoic. *Geobiology* **2012**, *10*, 298–310. [CrossRef]
39. Pagani, M.; Arthur, M.A.; Freeman, K.H. Miocene evolution of atmospheric carbon dioxide. *Paleoceanography* **1999**, *14*, 273–292. [CrossRef]
40. Mackay, D.; Shiu, W.Y. A critical review of Henry's law constants for chemicals of environmental interest. *J. Phys. Chem. Ref. Data* **1981**, *10*, 1175–1199. [CrossRef]
41. Staudinger, J.; Roberts, P.V. A critical review of Henry's law constants for environmental applications. *Crit. Rev. Environ. Sci. Technol.* **1996**, *26*, 205–297. [CrossRef]
42. Clever, H.L. An Evaluation of the Solubility of Carbon Dioxide in Aqueous Electrolyte Solutions. In *IUPAC-NIST Solubility Database: NIST Standard Reference Database 106*; Scharlin, P., Ed.; 1996, Office of Data and Informatics of the National Institute of Standards and Technology (NIST); Material Measurement Laboratory (MML): Washington, DC, USA, 2023; 94p.
43. Sander, R. Compilation of Henry's law constants (version 5.0.0) for water as solvent. *Atmos. Chem. Phys.* **2023**, *23*, 10901–12440. [CrossRef]
44. Abbatt, J.D.P. *Section 5. Heterogeneous Processes, in Chemical Kinetics and Photochemical Data for Use in Atmospheric Studies*; Burkholder, J.B., Sander, S.P., Eds.; JPL Publication No., 19-5; Jet Propulsion Laboratory: Pasadena, CA, USA, 2019.
45. Scharlin, P.; Cargill, R.W. *Carbon Dioxide in Water and Aqueous Electrolyte Solutions*; Lorimer, J.W., Ed.; IUPAC Solubility Data Series; International Union of Pure and Applied Chemistry: Oxford, UK, 1996; Volume 62, pp. xviii + 383.
46. Sazonov, V.P.; Shaw, D.G. *Solubility System: Carbon dioxide with Electrolyte and Water, in IUPAC-NIST Solubility Database: NIST Standard Reference Database 106, Volume 62*; Scharlin, P., Ed.; Oxford University Press: Oxford, UK, 1996.
47. Weiss, R. Carbon dioxide in water and seawater: The solubility of a non-ideal gas. *Mar. Chem.* **1974**, *2*, 203–215. [CrossRef]

48. Kozdon, R.; Kelly, D.C.; Kita, N.T.; Fournelle, J.H.; Valley, J.W. Planktonic foraminiferal oxygen isotope analysis by ion microprobe technique suggests warm tropical sea surface temperatures during the Early Paleogene. *Paleoceanography* **2011**, *26*, PA3206. [CrossRef]
49. Gaskell, D.E.; Huber, M.; O'brien, C.L.; Inglis, G.N.; Acosta, R.P.; Poulsen, C.J.; Hull, P.M. The latitudinal temperature gradient and its climate dependence as inferred from foraminiferal $\delta^{18}O$ over the past 95 million years. *Proc. Natl. Acad. Sci. USA* **2022**, *119*. [CrossRef] [PubMed]
50. Bernard, S.; Daval, D.; Ackerer, P.; Pont, S.; Meibom, A. Burial-induced oxygen-isotope re-equilibration of fossil foraminifera explains ocean paleotemperature paradoxes. *Nat. Commun.* **2017**, *8*, 1134. [CrossRef]
51. Lüthi, D.; Le Floch, M.; Bereiter, B.; Blunier, T.; Barnola, J.-M.; Siegenthaler, U.; Raynaud, D.; Jouzel, J.; Fischer, H.; Kawamura, K.; et al. High-resolution carbon dioxide concentration record 650,000–800,000 years before present. *Nature* **2008**, *453*, 379–382. [CrossRef]
52. Lüthi, D.; Le Floch, M.; Bereiter, B.; Blunier, T.; Barnola, J.-M.; Siegenthaler, U.; Raynaud, D.; Jouzel, J.; Fischer, H.; Kawamura, K.; et al. EPICA Dome C Ice Core Terminations I and II Air Isotopes and CO_2 Data. 2013; This Dataset Gathers Published and New Data of d15N, d18Oatm and CO_2 from the EPICA Dome C Ice Core over Terminations I and II. Available online: https://www.ncei.noaa.gov/pub/data/paleo/icecore/antarctica/epica_domec/edc2013d18oatm.txt (accessed on 23 March 2024).
53. EEA. Trends in Atmospheric Concentrations of CO2 (ppm), CH4 (ppb) and N2O (ppb), between 1800 and 2017. *Data Visualizations 2024.* Available online: https://www.eea.europa.eu/data-and-maps/daviz/atmospheric-concentration-of-carbon-dioxide-5/download.table (accessed on 28 March 2024).
54. Wu, B.; Woodward, M.D.; Nishio, S.; Olivieri, A.; Rojas, L.P.; van Rijsbergen, M.; Derradji-Aouat, A. Fresh Water and Seawater Properties. In *26th International Towing Tank Conference*; ITCC Association: Rio de Janeiro, Brazil, 2011.
55. Carroll, J.J.; Slupsky, J.D.; Mather, A.E. The Solubility of Carbon Dioxide in Water at Low Pressure. *J. Phys. Chem. Ref. Data* **1991**, *20*, 1201–1209. [CrossRef]
56. Pawlowicz, R. Key Physical Variables in the Ocean: Temperature, Salinity, and Density. *Nat. Educ. Knowl.* **2013**, *4*, 13. Available online: https://www.nature.com/scitable/knowledge/library/key-physical-variables-in-the-ocean-temperature-102805293/ (accessed on 28 August 2024).
57. Millero, F.J. The Partial Molal Volumes of Ions in Seawater1. *Limnol. Oceanogr.* **1969**, *14*, 376–385. [CrossRef]
58. Xian, P.; Ji, B.; Bian, S.; Zong, J.; Zhang, T. Influence of Differences in the Density of Seawater on the Measurement of the Underwater Gravity Gradient. *Sensors* **2023**, *23*, 714. [CrossRef]
59. Puigdomenech, I. Medusa: Chemical Equilibrium Software. 2004. Available online: https://www.kth.se/che/medusa/downloads-1.386254 (accessed on 28 August 2024).
60. Bijl, P.K.; Schouten, S.; Sluijs, A.; Reichart, G.-J.; Zachos, J.C.; Brinkhuis, H. Early Palaeogene temperature evolution of the southwest Pacific Ocean. *Nature* **2009**, *461*, 776–779. [CrossRef]
61. Huang, B.; Thorne, P.W.; Banzon, V.F.; Boyer, T.; Chepurin, G.; Lawrimore, J.H.; Menne, M.J.; Smith, T.M.; Vose, R.S.; Zhang, H.-M. Extended Reconstructed Sea Surface Temperature, Version 5 (ERSSTv5): Upgrades, Validations, and Intercomparisons. *J. Clim.* **2017**, *30*, 8179–8205. [CrossRef]
62. Huang, B. NOAA Extended Reconstructed Sea Surface Temperature (ERSST), Version 5.202402. 2017. Available online: https://www.ncei.noaa.gov/products/extended-reconstructed-sst (accessed on 2 April 2024).
63. Kennedy, J.J.; Rayner, N.A.; Atkinson, C.P.; Killick, R.E. An Ensemble Data Set of Sea Surface Temperature Change From 1850: The Met Office Hadley Centre HadSST.4.0.0.0 Data Set. *J. Geophys. Res. Atmos.* **2019**, *124*, 7719–7763. [CrossRef]
64. Ronov, A.B. The Distribution of Basalts, Andesites, and Rhyolites on the Continents and Continental Margins and in the Oceans. *Int. Geol. Rev.* **1985**, *27*, 1276–1284. [CrossRef]
65. Ernst, R.E.; Bond, D.P.G.; Zhang, S.-H.; Buchan, K.L.; Grasby, S.E.; Youbi, N.; Bilali, H.E.; Bekker, A.; Doucet, L.S. Large Igneous Province Record through Time and Implications for Secular Environmental Changes and Geological Time-Scale Boundaries. In *Large Igneous Provinces*; American Geophysical Union and John Wiley and Sons, Inc.: Hoboken, NJ, USA, 2021; pp. 1–26.
66. Percival, L.M.E.; Matsumoto, H.; Callegaro, S.; Erba, E.; Kerr, A.C.; Mutterlose, J.; Suzuki, K. Cretaceous large igneous provinces: From volcanic formation to environmental catastrophes and biological crises. *Geol. Soc. Lond. Spéc. Publ.* **2024**, *544*, sp544–sp2023. [CrossRef]
67. White, R.S.; McKenzie, D. Magmatism at rift zones: The generation of volcanic continental margins and flood basalts. *J. Geophys. Res.* **1989**, *94*, 7685–7729. [CrossRef]
68. Saunders, A.D.; Fitton, J.F.; Kerr, A.C. The North Atlantic Igneous Province. In *Large Igneous Provinces: Continental, Oceanic and Planetary Flood Volcanism*; Mahoney, J.J., Coffin, M.F., Eds.; American Geophysical Union Monograph: Washington, DC, USA, 1997; pp. 45–93.
69. Eldholm, O.; Grue, K. North Atlantic volcanic margins: Dimensions and production rates. *J. Geophys. Res.* **1994**, *99*, 2955–2968. [CrossRef]
70. Eldholm, O.; Myhre, A.M.; Thiede, J. *Cenozoic Tectono-Magmatic Events in the North Atlantic: Potential Paleoenvironmental Implications*; Springer: Berlin/Heidelberg, Germany, 1994.

71. Horni, J.; Hopper, J.R.; Blischke, A.; Geisler, W.H.; Stewart, M.; McDermott, K.; Judge, M.; Erlendsson, Ö.; Árting, U. Regional distribution of volcanism within the North Atlantic Igneous Province. In *The NE Atlantic Region. A Reappraisal of Crustal Structure, Tectonostratigraphy and Magmatic Evolution*; Péron-Pinvidic, G., Hopper, J.R., Funck, T., Stoker, M.S., Gaina, C., Doornenbal, J.C., Arting, U.E., Eds.; Geological Society, London, Special Publications: London, UK, 2017; p. SP447.18.
72. Ganerød, M.; Smethurst, M.A.; Torsvik, T.H.; Prestvik, T.; Rousse, S.; McKenna, C.; Van Hinsbergen, D.J.J.; Hendriks, B.W.H. The North Atlantic Igneous Province reconstructed and its relation to the Plume Generation Zone: The Antrim Lava Group revisited. *Geophys. J. Int.* **2010**, *182*, 183–202. [CrossRef]
73. Fukuyama, H. Heat of fusion of basaltic magma. *Earth Planet. Sci. Lett.* **1985**, *73*, 407–414. [CrossRef]
74. Millero, F.J.; Perron, G.; Desnoyers, J.E. Heat capacity of seawater solutions from 5° to 35 °C and 0.5 to 22‰ chlorinity. *J. Geophys. Res.* **1973**, *78*, 4499–4507. [CrossRef]
75. Shiklomanov, I.A. *World Fresh Water Resources, in Water in Crisis: A Guide to the World's Fresh Water Resources*; Gleik, P.H., Ed.; Oxford University: New York, NY, USA, 1993; pp. xxiv, 473.
76. Sparks, R.S.J.; Huppert, H.E. Density changes during the fractional crystallization of basaltic magmas: Fluid dynamic implications. *Contrib. Miner. Pet.* **1984**, *85*, 300–309. [CrossRef]
77. Green, D.H.; Falloon, T.J.; Eggins, S.M.; Yaxley, G.M. Primary magmas and mantle temperatures. *Eur. J. Miner.* **2001**, *13*, 437–451. [CrossRef]
78. Bouhifd, M.A.; Besson, P.; Courtial, P.; Gérardin, C.; Navrotsky, A.; Richet, P. Thermochemistry and melting properties of basalt. *Contrib. Miner. Pet.* **2007**, *153*, 689–698. [CrossRef]
79. Rae, J.W.; Foster, G.L.; Schmidt, D.N.; Elliott, T. Boron isotopes and B/Ca in benthic foraminifera: Proxies for the deep ocean carbonate system. *Earth Planet. Sci. Lett.* **2011**, *302*, 403–413. [CrossRef]
80. Rae, J.W.B. Boron Isotopes in Foraminifera: Systematics, Biomineralisation, and CO_2 Reconstruction. In *Boron Isotopes: The Fifth Element*; Marschall, H., Foster, G., Eds.; Springer International Publishing: Cham, Switzerland, 2018; pp. 107–143.
81. Rasbury, E.T.; Hemming, N.G. Boron Isotopes: A "Paleo-pH Meter" for Tracking Ancient Atmospheric CO_2. *Elements* **2017**, *13*, 243–248. [CrossRef]
82. Raitzsch, M.; Hönisch, B. Cenozoic boron isotope variations in benthic foraminifers. *Geology* **2013**, *41*, 591–594. [CrossRef]
83. Shao, J.; Stott, L.D.; Gray, W.R.; Greenop, R.; Pecher, I.; Neil, H.L.; Coffin, R.B.; Davy, B.; Rae, J.W. Atmosphere-Ocean CO_2 Exchange Across the Last Deglaciation From the Boron Isotope Proxy. *Paleoceanogr. Paleoclimatology* **2019**, *34*, 1650–1670. [CrossRef]
84. Zhang, Y.G.; Pearson, A.; Benthien, A.; Dong, L.; Huybers, P.; Liu, X.; Pagani, M. Refining the alkenone-pCO_2 method I: Lessons from the Quaternary glacial cycles. *Geochim. Cosmochim. Acta* **2019**, *260*, 177–191. Available online: https://www.sciencedirect.com/science/article/pii/S0016703719303813 (accessed on 22 July 2024). [CrossRef]
85. Zhang, Y.G.; Henderiks, J.; Liu, X. Refining the alkenone-pCO_2 method II: Towards resolving the physiological parameter 'b'. *Geochim. Cosmochim. Acta* **2020**, *281*, 118–134. [CrossRef]
86. Tanner, T.; Hernández-Almeida, I.; Drury, A.J.; Guitián, J.; Stoll, H. Decreasing Atmospheric CO_2 During the Late Miocene Cooling. *Paleoceanogr. Paleoclimatology* **2020**, *35*, e2020PA003925. [CrossRef]
87. Lisiecki, L.E. A benthic δ^{13}C-based proxy for atmospheric pCO_2 over the last 1.5 Myr. *Geophys. Res. Lett.* **2010**, *37*. [CrossRef]
88. Sachs, J.P.; Schneider, R.R.; Eglinton, T.I.; Freeman, K.H.; Ganssen, G.; McManus, J.F.; Oppo, D.W. Alkenones as paleoceanographic proxies. *Geochem. Geophys. Geosystems* **2000**, *1*. [CrossRef]
89. Seki, O.; Foster, G.L.; Schmidt, D.N.; Mackensen, A.; Kawamura, K.; Pancost, R.D. Alkenone and boron-based Pliocene pCO_2 records. *Earth Planet. Sci. Lett.* **2010**, *292*, 201–211. [CrossRef]
90. Foster, G.L.; Rae, J.W. Reconstructing Ocean pH with Boron Isotopes in Foraminifera. *Annu. Rev. Earth Planet. Sci.* **2016**, *44*, 207–237. [CrossRef]
91. Gaillardet, J.; Lemarchand, D. Boron in the Weathering Environment. In *Boron Isotopes: The Fifth Element*; Marschall, H., Foster, G., Eds.; Springer International Publishing: Cham, Switzerland, 2018; pp. 163–188.
92. Gradstein, F.M.; Ogg, J.G. Geologic Time Scale 2004—Why, how, and where next! *Lethaia* **2004**, *37*, 175–181. [CrossRef]
93. Bijl, P.K.; Houben, A.J.P.; Schouten, S.; Bohaty, S.M.; Sluijs, A.; Reichart, G.-J.; Damsté, J.S.S.; Brinkhuis, H. Transient Middle Eocene Atmospheric CO_2 and Temperature Variations. *Science* **2010**, *330*, 819–821. [CrossRef]
94. Schouten, S.; van der Meer, M.T.J.; Hopmans, E.C.; Rijpstra, W.I.C.; Reysenbach, A.-L.; Ward, D.M.; Damsté, J.S.S. Archaeal and bacterial glycerol dialkyl glycerol tetraether lipids in hot springs of yellowstone national park. *Appl. Environ. Microbiol.* **2007**, *73*, 6181–6191. [CrossRef]
95. Tateo, F. Clay Minerals at the Paleocene–Eocene Thermal Maximum: Interpretations, Limits, and Perspectives. *Minerals* **2020**, *10*, 1073. [CrossRef]
96. Martín-Martín, M.; Guerrera, F.; Tosquella, J.; Tramontana, M. Paleocene-Lower Eocene carbonate platforms of westernmost Tethys. *Sediment. Geol.* **2020**, *404*, 105674. [CrossRef]
97. Li, J.; Hu, X.; Garzanti, E.; BouDagher-Fadel, M. Spatial heterogeneity in carbonate-platform environments and carbon isotope values across the Paleocene–Eocene thermal maximum (Tethys Himalaya, South Tibet). *Glob. Planet. Chang.* **2022**, *214*, 103853. [CrossRef]
98. Bowen, G.J.; Zachos, J.C. Rapid carbon sequestration at the termination of the Palaeocene–Eocene Thermal Maximum. *Nat. Geosci.* **2010**, *3*, 866–869. [CrossRef]

99. Bains, S.; Norris, R.D.; Corfield, R.M.; Faul, K.L. Termination of global warmth at the Palaeocene/Eocene boundary through productivity feedback. *Nature* **2000**, *407*, 171–174. [CrossRef]
100. Bains, S.; Norris, R.D.; Corfield, R.; Bowen, G.J.; Gingerich, P.D.; Koch, P.L. Marine-terrestrial linkages at the Paleocene-Eocene boundary. In *Causes and Consequences of Globally Warm Climates in the Early Paleogene*; Geological Society of America: Boulder, CO, USA, 2003; pp. 1–9.
101. Steinthorsdottir, M.; Coxall, H.K.; de Boer, A.M.; Huber, M.; Barbolini, N.; Bradshaw, C.D.; Burls, N.J.; Feakins, S.J.; Gasson, E.; Henderiks, J.; et al. The Miocene: The Future of the Past. *Paleoceanogr. Paleoclimatology* **2021**, *36*, e2020PA004037. [CrossRef]
102. Yang, Y.; Ye, C.; Galy, A.; Fang, X.; Xue, Y.; Liu, Y.; Yang, R.; Zhang, R.; Han, W.; Zhang, W.; et al. Monsoon-Enhanced Silicate Weathering as a New Atmospheric CO_2 Consumption Mechanism Contributing to Fast Late Miocene Global Cooling. *Paleoceanogr. Paleoclimatology* **2021**, *36*, e2020PA004008. [CrossRef]
103. Pélissié, T.; Orliac, M.J.; Antoine, P.O.; Biot, V.; Escarguel, G. Beyond Eocene and Oligocene Epochs: The Causses du Quercy Geopark and the Grande Coupure. *Geoconservation Res.* **2023**, *4*, 573–585. [CrossRef]
104. Kürschner, W.M.; Kvaček, Z.; Dilcher, D.L. The impact of Miocene atmospheric carbon dioxide fluctuations on climate and the evolution of terrestrial ecosystems. *Proc. Natl. Acad. Sci. USA* **2008**, *105*, 449–453. [CrossRef]
105. Barker, P.; Thomas, E. Origin, signature and palaeoclimatic influence of the Antarctic Circumpolar Current. *Earth-Sci. Rev.* **2004**, *66*, 143–162. [CrossRef]
106. Crowley, T.J. The geologic record of climatic change. *Rev. Geophys.* **1983**, *21*, 828–877. [CrossRef]
107. Culberson, C.H.; Pytkowicz, R.M. Ionization of water in seawater. *Mar. Chem.* **1973**, *1*, 309–316. [CrossRef]
108. Bauska, T.K.; Joos, F.; Mix, A.C.; Roth, R.; Ahn, J.; Brook, E.J. Links between atmospheric carbon dioxide, the land carbon reservoir and climate over the past millennium. *Nat. Geosci.* **2015**, *8*, 383–387. [CrossRef]
109. Teng, H.; Masutani, S.; Kinoshita, C.; Nihous, G. Solubility of CO_2 in the ocean and its effect on CO_2 dissolution. *Energy Convers. Manag.* **1996**, *37*, 1029–1038. [CrossRef]
110. Tachikawa, K.; Vidal, L.; Sonzogni, C.; Bard, E. Glacial/interglacial sea surface temperature changes in the Southwest Pacific ocean over the past 360ka. *Quat. Sci. Rev.* **2009**, *28*, 1160–1170. [CrossRef]
111. Hoffman, J.S.; Clark, P.U.; Parnell, A.C.; He, F. Regional and global sea-surface temperatures during the last interglaciation. *Science* **2017**, *355*, 276–279. [CrossRef] [PubMed]
112. Cuffey, K.M.; Clow, G.D.; Steig, E.J.; Buizert, C.; Fudge, T.J.; Koutnik, M.; Waddington, E.D.; Alley, R.B.; Severinghaus, J.P. Deglacial temperature history of West Antarctica. *Proc. Natl. Acad. Sci. USA* **2016**, *113*, 14249–14254. [CrossRef] [PubMed]
113. He, T.; Kemp, D.B.; Li, J.; Ruhl, M. Paleoenvironmental changes across the Mesozoic–Paleogene hyperthermal events. *Glob. Planet. Chang.* **2023**, *222*, 104058. [CrossRef]
114. Rampino, M.R.; Caldeira, K.; Rodriguez, S. Cycles of ∼32.5 My and ∼26.2 My in correlated episodes of continental flood basalts (CFBs), hyper-thermal climate pulses, anoxic oceans, and mass extinctions over the last 260 My: Connections between geological and astronomical cycles. *Earth-Sci. Rev.* **2023**, *246*, 104548. [CrossRef]
115. O'Brien, C.L.; Robinson, S.A.; Pancost, R.D.; Damsté, J.S.S.; Schouten, S.; Lunt, D.J.; Alsenz, H.; Bornemann, A.; Bottini, C.; Brassell, S.C.; et al. Cretaceous sea-surface temperature evolution: Constraints from TEX86 and planktonic foraminiferal oxygen isotopes. *Earth-Sci. Rev.* **2017**, *172*, 224–247. [CrossRef]
116. Moriya, K. Development of the Cretaceous Greenhouse Climate and the Oceanic Thermal Structure. *Paléontol. Res.* **2011**, *15*, 77–88. [CrossRef]
117. Huber, B.T.; MacLeod, K.G.; Watkins, D.K.; Coffin, M.F. The rise and fall of the Cretaceous Hot Greenhouse climate. *Glob. Planet. Chang.* **2018**, *167*, 1–23. [CrossRef]
118. Hoffman, P.F.; Schrag, D.P. The snowball Earth hypothesis: Testing the limits of global change. *Terra Nova* **2002**, *14*, 129–155. [CrossRef]
119. Joseph, A. Chapter 2—Geological timeline of significant events on Earth. In *Water Worlds in the Solar System*; Joseph, A., Ed.; Elsevier: Amsterdam, The Netherlands, 2023; pp. 55–114.
120. Dutkiewicz, A.; Merdith, A.S.; Collins, A.S.; Mather, B.; Ilano, L.; Zahirovic, S.; Müller, R.D. Duration of Sturtian "Snowball Earth" glaciation linked to exceptionally low mid-ocean ridge outgassing. *Geology* **2024**, *52*, 292–296. [CrossRef]
121. Parmentola, J. Celestial Mechanics and Estimating the Termination of the Holocene Warm Period. *Sci. Clim. Chang.* **2023**, *3*, 392–395. [CrossRef]
122. Lindzen, R.S.; Pan, W. A note on orbital control of equator-pole heat fluxes. *Clim. Dyn.* **1994**, *10*, 49–57. [CrossRef]
123. Wunsch, C. The spectral description of climate change including the 100 ky energy. *Clim. Dyn.* **2003**, *20*, 353–363. [CrossRef]
124. Petit, J.R.; Jouzel, J.; Raynaud, D.; Barkov, N.I.; Barnola, J.M.; Basile, I.; Bender, M.; Chappellaz, J.; Davis, M.; Delaygue, G.; et al. Climate and atmospheric history of the past 420,000 years from the Vostok ice core, Antarctica. *Nature* **1999**, *399*, 429–436. [CrossRef]

Disclaimer/Publisher's Note: The statements, opinions and data contained in all publications are solely those of the individual author(s) and contributor(s) and not of MDPI and/or the editor(s). MDPI and/or the editor(s) disclaim responsibility for any injury to people or property resulting from any ideas, methods, instructions or products referred to in the content.